Forced and internal variability of tropical cyclone track density in the western North Pacific

Wei Mei * and Shang-Ping Xie

Scripps Institution of Oceanography, University of California at San Diego, La Jolla, California

Ming Zhao

NOAA/Geophysical Fluid Dynamics Laboratory, Princeton, New Jersey, and University Corporation for Atmospheric Research, Boulder, Colorado

Yuqing Wang

International Pacific Research Center, and Department of Meteorology, University of Hawaii at Manoa, Honolulu, Hawaii

* *Corresponding author address:* Wei Mei, Scripps Institution of Oceanography, University of California at San Diego, 9500 Gilman Drive #0206, La Jolla, CA 92093-0206, USA.
E-mail: wmei@ucsd.edu

ABSTRACT

Forced interannual-to-decadal variability of annual tropical cyclone (TC) track density in the western North Pacific between 1979-2008 is studied using TC tracks from observations and simulations by a 25-km-resolution version of the GFDL High-Resolution Atmospheric Model (HiRAM) that is forced by observed sea surface temperatures (SSTs). Two modes dominate the decadal variability: a nearly-basin-wide mode, and a dipole mode between the subtropics and lower latitudes. The former mode links to variations in TC number and is forced by SST variations over the off-equatorial tropical central North Pacific, whereas the latter might be associated with the Atlantic Multidecadal Oscillation. The interannual variability is also controlled by two modes: a basin-wide mode driven by SST anomalies of opposite signs located respectively in the tropical central Pacific and eastern Indian Ocean, and a southeast-northwest dipole mode connected to the conventional eastern Pacific ENSO. The seasonal evolution of the ENSO effect on TC activity is further explored via a joint EOF analysis using TC track density of consecutive seasons, and the analysis reveals that two types of ENSO are at work.

Internal variability in TC track density is then examined using ensemble simulations from both HiRAM and a regional atmospheric model. It exhibits prominent spatial and seasonal patterns, and it is particularly strong in the South China Sea and along the coast of East Asia. This makes an accurate prediction and projection of TC landfall extremely challenging in these regions. In contrast, basin-integrated metrics (e.g., total TC counts and TC days) are more predictable.

1. Introduction

The western North Pacific (WNP) is the basin where tropical cyclones (TCs) are most active. On average it witnesses more than 1/3 of global TCs, some being the strongest TCs in individual years. These, together with the large and dense population in East and Southeast Asia, have motivated numerous efforts to understand the variability of WNP TCs (e.g., Chan 1985; Lander 1994; Wang and Chan 2002; Chia and Ropelewski 2002; Elsner and Liu 2003; Wu et al. 2004; Camargo and Sobel 2005; Camargo et al. 2007a,b; Liu and Chan 2008; Zhan et al. 2011a; Kim et al. 2011a; Huang et al. 2011; Wu et al. 2012; Park et al. 2013).

Among the many metrics of TC activity, track density is directly related to the TC-caused damage to human society by landfall. Its variability integrates variations in the number and location of TC genesis and in TC tracks. The WNP TC *number* varies considerably on various timescales. On relatively long timescales, available TC best-track data show that the WNP TC number peaked in the mid-1960s and early 1990s with a period of around 23 years (Matsuura et al. 2003). This interdecadal variability is related to the low-frequency variations in sea surface temperatures (SSTs) over the tropical central Pacific via the modulation of westerlies of the monsoon trough over the WNP. Recently, Liu and Chan (2013) show that the number of TCs generated over the southeastern part of the WNP is significantly related to the Pacific Decadal Oscillation (PDO). Meanwhile, the TC number exhibits short-term variations (Chan and Shi 1996), but the underlying mechanism is unclear. Some studies have concluded that annual TC number does not correlate with the El Niño-Southern Oscillation (ENSO) (e.g., Lander 1994; Wang and Chan 2002; Camargo and Sobel 2005).

Although no connections have been reported between the total TC counts and ENSO, numerous studies have shown that ENSO strongly modulates the *geographical distribution* of TC genesis. During El Niño years, TCs tend to form closer to the equator and the dateline (i.e., more frequent in the southeastern quadrant of the WNP) than during La Niña years (Wang and Chan 2002; Camargo and Sobel 2005; Kim et al. 2010, 2011a), owing to the eastward extension of monsoon trough in the WNP. These storms, on average, persist longer and can grow to higher intensities than those during La Niña years as they pass over a larger area of warm water that provides energy for their development (Wang and Chan 2002; Camargo and Sobel 2005). As a result, significantly more intense typhoons and fewer storms of tropical storm intensity are found for El Niño states (Camargo and Sobel 2005).

Steered largely by large-scale environmental air flows, TCs generally move in a direction between westward and northward after their formation, and the resultant *tracks* exhibit strong variations. TC tracks over the WNP can be grouped into one of the following two categories: straight-moving and recurving (Lander 1996; Elsner and Liu 2003). Including information of other aspects such as genesis location, TC tracks can be divided into further more types. For example, Camargo et al. (2007a) classify the WNP TCs over the entire TC season into seven clusters with a very detailed discussion. They reveal that straight-moving clusters are tighter than recurving clusters in latitudinal direction. Two of the seven clusters may be linked to El Niño conditions while one cluster occurs more frequently during La Niña events (Camargo et al. 2007b). Using a different clustering technique, Kim et al. (2011b) show that the WNP TC tracks over the TC active season can also be categorized into seven clusters with four of them being linked to either ENSO or the quasi-biennial oscillation.

Because of the large variability in its three contributors (i.e., count, genesis location, and track), we expect to see strong variations in TC *track density* over the WNP. Compared to 1951-1979, Ho et al. (2004) find that during 1980-2001 TC track density of the boreal summertime significantly decreased over the East China Sea and Philippine Sea while had a slight increase in the South China Sea (SCS). They connect these interdecadal changes to the westward expansion of the subtropical WNP High. More recently, Liu and Chan (2008) explore the low-frequency variability of TC track density using an empirical orthogonal function (EOF) analysis, and identify three leading modes, two of which are linked to variations in large-scale flow patterns. They attribute part of the decadal variability in TC track density to the PDO.

On interannual timescales, owing to the influence of ENSO on the position of TC genesis and tracks, it is natural to look into its effect on TC track density. Indeed, Wang and Chan (2002) find that during strong El Niño years, TC track density almost doubles that in strong La Niña years. Recently, there is much debate about the two types of ENSO: the central Pacific (CP) and the conventional eastern Pacific (EP) ENSO (Ashok et al. 2007; Kao and Yu 2009; Kug et al. 2009). They appear to affect TC track density differently (Kim et al. 2011a; Wang et al. 2013). For example, during the peak TC season, the EP warming produces a southeast-northwest dipole pattern in TC track density with below-normal activity over the northwestern part of the basin and reduced landfall on the coasts of East Asia. On the other hand, the CP warming favors above-normal activity over much of the WNP, including the northwestern flank where landfall takes place.

The above-mentioned studies, primarily based on observations, have greatly advanced our knowledge of the spatial and temporal variability in TC track density, the underlying patterns of atmospheric circulation, and its possible links to SSTs. Observations of short duration alone, however, cannot establish a cause-effect relationship between TC activity and SSTs. Here we take advantage of numerical simulations from high-resolution atmospheric general circulation models (AGCMs) forced by observed SSTs that show skills in reproducing interannual variability in TC counts. We show that the skills extend to TC track density variability. By design, the model skills are due to the prescribed SST variability, allowing us to isolate patterns of SST forcing for TC variability. While previous studies on how ENSO conditions affect TC track density heavily rely on correlation, regression, and composite analyses, we use EOF analyses – a more objective method – to extract the dominant modes of the variability in TC track density, and then connect these modes to the underlying SST forcing. We also, for the first time, explore the internal variability in WNP TC track density using the high-resolution ensemble simulations, with important implications for the predictability of local TC occurrence.

After describing observational TC data, numerical simulations and methods (section 2), in section 3 we study separately the low- and high-frequency variability of the WNP TC track density and explore underlying mechanisms by analyzing SSTs and various atmospheric fields. We also study, in section 3, the seasonal evolution of ENSO effect on TC activity via a joint EOF analysis of TC track density during consecutive seasons. Section 4 examines the internal variability and associated predictability of the WNP TC track density and landfall using both global and regional downscaling simulations. A summary is given in section 5.

2. Data and Methods

a. Observational and reanalysis data

The observed WNP TC tracks are from the Joint Typhoon Warning Center best track dataset (Chu et al. 2002), which provides the location and intensity of TCs at 6-hr intervals since 1945. SSTs from the Hadley Centre Sea Ice and Sea Surface Temperature data set (HadISST; Rayner et al. 2003) and atmospheric variables (including sea level pressure, 850- and 200-hPa winds and 500-hPa pressure velocity) from the NCEP/NCAR Reanalysis 1 (Kalnay et al. 1996) are employed to understand the possible mechanisms underlying the variability in observed TC track density[1]. To be consistent with the simulations described below, only the observational data from 1979 through 2008 are used.

b. *HiRAM simulations*

We use TC tracks simulated by a 25-km-resolution version of the Geophysical Fluid Dynamics Laboratory (GFDL) High-Resolution Atmospheric Model (HiRAM; Zhao et al. 2012) to explore both the forced and internal variability of TC track density. The model is forced by observed SSTs, following the procedure of the Atmospheric Model Intercomparison Project (AMIP), with various modes of climate variability (such as ENSO and PDO) being imprinted in the SST anomalies. The simulations consist of three members, which are different only in initial conditions. The difference among the member runs is due to the chaotic and nonlinear nature of the atmospheric processes (Harzallah and Sadourny 1995; Griffies and Bryan 1997). The ensemble mean, representing a reproducible signal in association with external forcing, is considered as an approximation of the *forced* response in TC activity to prescribed SSTs.[2] The deviation of each member from the ensemble mean is viewed as an approximation of the *internal* variability of the model.

The criteria and methods used for detecting and tracking TCs are described in Mei et al. (2014), and are presented here in Appendix A for the convenience of reference.

As shown in Mei et al. (2014), HiRAM generally reproduces the spatial distribution of global TC genesis and tracks (see also Fig. 1 here for TCs over the WNP), well simulates the climatological TC counts in all TC active basins, and is able to capture the interannual-to-decadal variations in TC counts over the North Atlantic. Figure 2a compares the evolution of anomalous annual TC counts over the WNP between observations and HiRAM simulations. It is evident that HiRAM reasonably well simulates the observed variability in annual TC number, particularly on the low-frequency timescales. For example, on decadal timescales, the TC number maximized during the early 1990s in both observations and HiRAM simulations. The model overestimates the interannual variations during the first 10 years of the

[1]Using NCEP-DOE Reanalysis 2 data produces nearly identical results.

[2]A strictly defined forced response can be obtained following the methodology presented in Venzke et al. (1999) when the ensemble size is greater than 10. But in this study with only three (HiRAM) simulations we simply define their ensemble mean as the forced response. Similarly, three members may not be sufficient to represent internal variability accurately. Further studies with a much larger ensemble size are desirable in the future.

simulations. This bias may be due to the lack of short-timescale air-sea coupling, an issue that needs further investigation and deeper understanding.

Figures 3a,b compare the observed and HiRAM-simulated geographical distribution of climatological annual TC track density. Generally, HiRAM reproduces the observed large-scale pattern and magnitude of the track density. For instance, in both observations and HiRAM simulations, TC track density is relatively dense over the East China Sea and the Philippine Sea with a southeast-northwest orientation, which corresponds a typical TC motion. But HiRAM underestimates the track density over the SCS, which, to a large extent, can be attributed to a severe underestimation of TC genesis there (cf. Figs. 1a,b).

c. *iRAM simulations*

We also use regional downscaling simulations from the International Pacific Research Center (IPRC) Regional Atmospheric Model (iRAM) to study the *internal* variability of WNP TC track density. The iRAM simulations consist of four members that are different only in initial conditions, and cover the period between 1982 and 2001. These simulations are constrained by observed atmospheric conditions on the lateral boundaries. Because of this and the short period of simulation (1982-2001), we do not use these simulations to explore the SST-forced response in TC activity. Instead, we *only* use deviations of the four-member simulations from the ensemble mean to understand the effects of downscaling on the *internal* variability of simulated TC track density.

Detailed descriptions of iRAM and the procedures for identifying TCs in iRAM are given in Wu et al. (2012), and are presented here in Appendix B for the convenience of reference. Wu et al. (2012) show that iRAM reproduces various aspects of the observed TCs, including the interannual and seasonal variations in TC counts. Figures 1c and 3c respectively show the spatial distribution of climatological TC genesis and tracks and track density between July and October downscaled by iRAM (see also Figs. 3 and 4e in Wu et al. 2012). It is clear that iRAM is also in general able to capture the climatological characteristics of the observed TC track density. In contrast to HiRAM, iRAM simulates too high TC activity over the SCS.

d. Methods

The TC track density in both observations and simulations is calculated as TC days within each $8^\circ \times 8^\circ$ grid within the WNP on a yearly or seasonal basis. (This large grid is used to reduce the noise level; using a smaller grid, such as $5^\circ \times 5^\circ$, produces similar results.) An EOF analysis is employed to extract the leading modes of the variability in TC track density, and linear correlation and regression analyses are utilized to detect the signal in SSTs and atmospheric conditions associated with each identified mode. A global mean SST (averaged between 65°S and 65°N) is removed before performing the correlation and regression analyses. Without removing the mean SST leads to similar results.

TCs can form in any month of the year over the WNP. In this study, we consider not only the annually integrated TC track density, but also the TC activity in different seasons. Based on the strength of the TC activity, we define three seasons, namely April-May-June (AMJ), July-August-September (JAS), and October-November-December (OND), respectively as the early, peak, and late TC seasons.

3. Forced variability in TC track density

We use observed and HiRAM-simulated TC tracks to study the forced variability of WNP TC track density, separately on decadal and interannual timescales because of the difference in the underlying mechanisms. We separate out these two timescales via a 10-yr-band-pass filter following Liu and Chan (2008) and using the Fast Fourier Transform technique. In this section, we first examine separately the low- and high-frequency components of annual TC track density, and then proceed to explore the seasonal evolution of ENSO effect on TC track density.

a. Low-frequency variability of annual TC track density

In both observations and HiRAM simulations, the first leading mode of the low-frequency TC track density features a nearly-basin-wide pattern (Figs. 4a,b). The exception is the region right east of Taiwan in observations and extending from east of the Philippines north-to-northwestward through East China in simulations where track density varies in an opposite way to that over the rest of the WNP. The time series of the principal component (PC) shows that the basin-integrated activity peaked in the early 1990s (Fig. 4c). It almost overlaps with the time series of the normalized low-frequency TC counts in both observations and HiRAM simulations (Fig. 4c), indicating that this basin-wide mode is largely controlled by variations in annual TC number. This mode shows some resemblance to both the first and third modes of Liu and Chan (2008), but because the TC occurrence rate is normalized by the annual TC counts prior the EOF analysis, they obtain spatial patterns of an oscillation between the subtropics and lower latitudes (see Fig. 1 in Liu and Chan 2008).

Regressing global SSTs on the PC reveals that changes in surface temperatures over the off-equatorial tropical central North Pacific may be responsible for this mode with anomalous warming corresponding to above-normal WNP TC activity (Fig. 5a for HiRAM simulations and Fig. S1a in the supplementary material for observations). This is in line with Matsuura et al. (2003), who also find that in observations decadal variations of the SSTs over this region correlate with the low-frequency changes in WNP TC counts of the peak TC season although such a connection in their model is quite weak. The anomalously warm SSTs there induce, to its northwest, reduced SLP, strengthened cyclonic vorticity in low-level atmospheric circulation, and enhanced upward motion in mid-troposphere (Figs. 5b,c for HiRAM simulations and Figs. S1b,c in the supplementary material for observations), all of which are favorable for producing an active TC season in the WNP. Weakened vertical shear of horizontal winds is also noticeable between 160°E-160°W, 10-20°N, and thus may be partially responsible for the above-normal TC activity in this area.

This mode may, to some extent, be linked to the PDO (Fig. 4c), as suggested in previous studies (e.g., Liu and Chan 2008, 2013). This connection becomes more evident when data over a longer period are used. As shown in Fig. S2b of the supplementary material, the obtained PC well matches the TC-peak-season PDO index, except for the 1980s. In particular, the recent cooling phase of the PDO reduces the TC genesis over the southeastern part of the WNP (Liu and Chan 2013) and contributes to the decreased TC track density over the tropical WNP since the mid-1990s.

In addition, it is interesting to note that SSTs over the tropical and high-latitude North Atlantic (NA) are significantly below normal during an active WNP TC season (Fig. 5a and Fig. S1a in the supplementary material), and the North Atlantic Oscillation (NAO) during the preceding winter season is in its positive phase (Fig. 4c; Elsner and Kocher 2000; Mei et al. 2014). As a result, the atmospheric conditions in the WNP and NA are opposite in terms of being favorable for TC development (Figs. 5b,c and Figs. S1b,c in the supplementary material), and thus TC activity over these two basins is expected to vary in an opposite way. The physical mechanism for the connection between these two basins is unclear at this stage, and is worth further exploration.

The second mode in both observations and HiRAM simulations is characterized by a dipole pattern of TC activity over two latitudinal bands in 110°-150°E between 10°-20°N and 20°-30°N (dashed white boxes in Figs. 6a,b), although large discrepancies exist in the rest of the WNP between observations and simulations. The temporal evolution of this mode exhibits a phase shift around the mid-1990s with lower latitudes (i.e., 10°-20°N) experiencing below-normal TC activity after the shift (Fig. 6c). The timing of this phase shift coincides with the Atlantic Multidecadal Oscillation (AMO). This is further supported by the pattern of global SST anomalies regressed on the corresponding PC (Fig. 7a for HiRAM simulations and Fig. S3a in the supplementary material for observations). An examination of various atmospheric fields suggests that SLP, low-level vorticity and mid-level upward motion have the right anomalous pattern (Fig. 7b and Fig. S3b in the supplementary material); the role of vertical wind shear is quite weak. Although this mode resembles the second mode of Liu and Chan (2008) that is obtained using a longer period of data, this mode seems not as robust as the first mode discussed above, and our confidence in it is low. Further exploration of the underlying dynamics is needed, and simulations by an AGCM that is subject to an AMO-like anomalous SST pattern may shed light on this.

b. High-frequency variability of annual TC track density

Applying EOF analysis to the high-frequency component of observed WNP TC track density depicts only one physically-meaningful mode (Fig. 8a). This mode suggests that the TC activity over the open ocean varies in phase except over the southern SCS and along the south and east coast of China where the phase is opposite. This differs from the classic pattern of anomalous TC activity induced by the conventional EP ENSO that is characterized by an oscillation between the southeastern and northwestern quadrants of the WNP. This difference may be reconciled by the EOF analysis of HiRAM simulations that reveals two dominant modes (Figs. 8c,e). One mode (the first mode) features a basin-wide mode, and the other (the third mode) shows a dipole pattern in the southeast-northwest direction[3]. The first mode is closely related to variations in annual TC number as indicated

[3]Note that the second EOF mode in HiRAM simulations is not physically meaningful since its PC appears to be noise and no organized SST pattern can be associated with it. Similarly, the third leading mode in observations shows a dipole structure, but cannot be linked to any organized SST pattern. Accordingly,

by a high correlation coefficient between the PC of this mode and the time series of the high-frequency component of annual TC counts (the linear correlation coefficient r=0.92; Fig. 8d). The spatial pattern of the third mode of HiRAM simulations is quite similar to that of TC activity induced by the conventional EP ENSO (e.g., Wang and Chan 2002; Kim et al. 2011a). A linear combination of PCs of these two modes highly correlates with the PC of the dominant mode in observations (r=0.75; Fig. 8b), indicating that the leading mode extracted from observations may be considered as a mixture of the two modes of HiRAM simulations.

This is further confirmed by maps of global SSTs regressed respectively on PCs of the above-discussed modes. The first mode of HiRAM simulations (Fig. 9b) can be attributed to variations of SSTs over the tropical central Pacific and those over East Indian Ocean and western Pacific. The former SST anomalies are connected with the CP El Niño (Ashok et al. 2007; Kao and Yu 2009; Kug et al. 2009). Above-normal SSTs over the equatorial and northern off-equatorial tropical central Pacific and below-normal SSTs over the eastern tropical Indian Ocean are optimal for above-normal TC activity over the WNP, consistent with recent studies (e.g., Du et al. 2011; Zhan et al. 2011a,b; Kim et al. 2011a; Tao et al. 2012; Jin et al. 2013). The third mode of HiRAM simulations is in association with the conventional EP El Niño (Fig. 9c). The regressed anomalous SST pattern for the leading mode of observations (Fig. 9a) appears to be a superposition of the two SST patterns for model simulations (Figs. 9b,c).

To understand the underlying mechanisms, we further regressed atmospheric variables on PCs from HiRAM simulations. For the first mode, it appears that positive SST anomalies over the equatorial and northern off-equatorial tropical central Pacific and/or negative SST anomalies over the East Indian Ocean reduce SLP, increase low-level vorticity, and enhance mid-level upward motion and thus convection over the WNP (Figs. 10a,b), and thereby produce a favorable environment for the WNP TC genesis and development.

On the contrary, a conventional EP El Niño generates a southeast-northwest dipole pattern over the WNP in the above-mentioned atmospheric fields: the southeastern quadrant experiences below-normal SLP, above-normal low-level vorticity, and above-normal mid-level upward motion and corresponding convective activity (Figs. 10c,d), and hence above-normal TC activity (Fig. 8c); the northwestern quadrant witnesses opposite conditions.

For observations, the regressed atmospheric fields (i.e., the SLP, low-level vorticity and

these modes are not discussed further here.

mid-level upward motion; Fig. S4 in the supplementary material) have a consistent spatial distribution as the anomalies in TC track density shown in Fig. 8a, and can be viewed as a combination of the regressed fields for the two modes of HiRAM simulations shown in Fig. 10.

Similar to the situation on low-frequency timescales (section 3a), the role of vertical wind shear appears to be relatively minor – compared to other atmospheric variables such as low-level vorticity – in controlling WNP TC activity on interannual timescales since the overall spatial correlation between TC track density and vertical wind shear is low (e.g., cf. Figs. 8c,e and Figs. 10b,d). This is different from the situation in the NA, where all the factors discussed above (including vertical wind shear) work constructively to generate stronger TC activity when tropical NA SSTs are warmer than normal (Emanuel 2007; Vimont and Kossin 2007; Mei et al. 2014). Such a difference between basins is consistent with previous studies suggesting that vertical wind shear plays a more important role in TC activity over the NA than over the WNP (e.g., Aiyyer and Thorncroft 2011). At this stage the reason why the importance of vertical wind shear differs between these two basins is unclear and needs further investigation. One possible explanation is that relative humidity is higher and has weaker gradients in the WNP than in the NA (Fig. S5), making shear-induced drying/ventilation effect weaker in suppressing TCs in the former basin.

c. Seasonal evolution of the ENSO effect on TC track density

Above analyses have shown that on interannual timescales the variability of WNP TC track density is primarily controlled by SSTs over the equatorial Pacific in association with ENSO. Meanwhile, both the TC activity and ENSO have strong seasonal dependence. Thus it is expected that the spatial pattern of anomalous TC track density associated with ENSO evolves with season, which can have important implications for seasonal prediction of TC activity. To extract the seasonality, we employ a joint EOF analysis of TC track density over five successive seasons starting from AMJ of the current year through AMJ of the following year [these seasons are denoted respectively as AMJ(0), JAS(0), OND(0), JFM(1) and AMJ(1) with "0" and "1" in the parentheses respectively indicating the current and the following year][4]. The underlying physical basis for this analysis is the persistence of ENSO

[4]Removing one or two seasons from the joint EOF analysis produces very similar results in both observations and HiRAM simulations except removing both AMJ(0) and AMJ(1) in HiRAM simulations (since the forced response in HiRAM is relatively weak during JAS and OND as shown below).

signals from AMJ(0) to AMJ(1) (see e.g., Kug and Kang 2006; Du et al. 2009; Kosaka et al. 2013).

The left panels of Fig. 11 show the spatial pattern of the first leading mode of the observed TC track density from AMJ(0) through JAS(1) [the plot for JAS(1) is obtained by regressing on the PC of the first mode], and the right panels display the accompanied anomalies in SST and 850-hPa wind based on regression. Overall this mode appears to be mainly associated with the evolution of SST anomalies over the tropical central and eastern Pacific – the so-called hybrid central and eastern Pacific ENSO (Johnson 2013). The SST anomalies start to develop near the central tropical Pacific, and then quickly expand to the eastern tropical Pacific, followed by a slow decay.

During the early TC season of the El Niño developing year [i.e., AMJ(0); Figs. 11a,b], modest warming develops over the equatorial and northern off-equatorial tropical central Pacific, and induces a giant cyclonic anomaly in the low-level circulation nearly over the whole WNP with westerly anomalies over the western tropical Pacific. This promotes the genesis and growth of WNP TCs. Because TC activity primarily concentrates over the low latitudes during AMJ, the generated anomaly in TC track density is most prominent south of 20°N (Fig. 11a).

As the warming over the tropical Pacific strengthens and moves eastward in JAS(0), the anomaly in the low-level circulation also intensifies (Fig. 11d), accompanied by an eastward extension of the monsoon trough that is closely related to TC genesis (e.g., Ritchie and Holland 1999). This, together with the climatological poleward extension of TC activity during JAS, leads to above-normal TC track density over the majority of the WNP (Fig. 11c). Meanwhile, an anomalously anticyclonic circulation develops over the southern SCS and the Philippines (which is clearer in low-level vorticity field), suppressing TC genesis and thus TC track density there (Fig. 11c).

During OND(0), the tropical Pacific warming reaches its peak intensity and extends to the west coast of South America (Fig. 11f). Correspondingly, the cyclonic anomaly in the low-level circulation shifts eastward, and the newly emerged anticyclonic anomaly grows to a considerable amplitude, expands to the whole SCS, and extends northeastward to the east of Japan (Fig. 11f). This results in a dipole pattern in both the WNP TC genesis and track density, most prominently equatorward of around 25°N (Fig. 11e).

In the following two seasons (i.e., JFM(1) and AMJ(1); Figs. 11g,h,i,j), the warming over the tropical central Pacific persists and then begins to decay, and both the anticyclonic (located over the SCS and the Philippines) and cyclonic (located to the east of the anticyclonic one) circulation anomalies and accordingly the dipole pattern in TC track density sustain. But during JAS(1), the warming over the central tropical Pacific has significantly decayed while that over the eastern Pacific is still evident (Fig. 11l). The east-west dipole in both the low-level circulation and TC activity has changed to a south-north one (Figs. 11k,l).

Figure 12 shows the second leading mode obtained from the joint EOF analysis of the observed TC track density together with the associated anomalies in SST and low-level atmospheric circulation. Different from the first mode, the anomalous SST pattern is mainly related to the conventional EP ENSO. Specifically, the SST anomalies first emerge over both the central and eastern tropical Pacific, then develop without a significant shift, peak over the eastern Pacific, quickly decay during AMJ(1), and eventually switch to an opposite phase during JAS(1). The accompanied SST anomalies in the Indian Ocean also evolve differently from those in the first mode.

Differences in the location and amplitude of tropical Pacific warming as well as in the accompanied Indian Ocean SST features induce different responses in the TC track density. During AMJ of the developing year [i.e., AMJ(0); Fig. 12b], the center of the warm SST anomalies in the tropical Pacific is located more eastward than in the first mode. As a response, the low-level cyclonic circulation anomaly over the tropical WNP is also located closer to the dateline, accompanied by an anticyclonic anomaly to its west over the SCS. Because of the larger amplitude of the warming, the circulation also has a stronger response (cf. Figs. 11b, 12b). These characteristics are well imprinted in an east-west dipole pattern of TC track density with a larger amplitude (Fig. 12a).

In JAS(0), the tropical Pacific warming develops, particularly near the coast of South America, leading to a prominent meridional dipole in the low-level circulation anomaly over the WNP as a Rossby wave train (Fig. 12d). As a result, the TC genesis equatorward of $\sim$10°N significantly increases while the TC genesis to the north decreases (Fig. 12c). This dipole pattern is also evident in TC track density but with 20°N as the nodal latitude (Fig. 12c). It is worth noting that the Indian Ocean dipole (IOD) begins to develop (Fig. 12d). At the same time, the anomalously anticyclonic circulation over the SCS slightly shift equatorward and a cyclonic anomaly is discernible over the northern SCS.

The eastern tropical Pacific warming and the IOD keep strengthening during OND(0) (Fig. 12f), and the anticyclonic anomaly in the low-level circulation over the SCS extends northward and dominates over the whole SCS. This anticyclonic anomaly and the eastwardshifted and weakened cyclonic anomaly near the dateline form an east-west dipole over the tropical WNP. This dipole in circulation anomalies together with the seasonal retreat of TC activity to lower latitudes produces a pattern in TC track density similar to that in AMJ(0) (cf. Figs. 12a,e).

During JFM(1) (Fig. 12h), the tropical Pacific anomalous warming starts to decay and the IOD has changed to a basin-wide warming in the Indian Ocean. The anticyclonic component of the dipole in the low-level circulation expands and moves eastward to cover the whole tropical WNP (Watanabe and Jin 2002), resulting in basin-wide reduced TC activity (Fig. 12g). Meanwhile, the establishment of anomalous easterly wind over the western tropical Pacific (Annamalai et al. 2005) quickly diminishes the eastern tropical Pacific warming during AMJ(1) by generating upwelling oceanic Kelvin waves (Fig. 12j; Kug and Kang 2006). The Indian Ocean warming persists and sustains the anticyclonic anomaly in low-level winds over the WNP, which is unfavorable for TC activity (Fig. 12i).

In JAS(1) (Fig. 12l), the warming over the Indian Ocean shifts eastward (Du et al. 2009), and a La Niña state begins to develop over the central and eastern equatorial Pacific. The Indo-Pacific SST anomalies work together to intensify the anticyclonic low-level circulation anomaly equatorward of 20°N and at the same time induce a cyclonic anomaly south of Japan (Fig. 12l; Kosaka et al. 2013). This leads to a dipole pattern in TC track density with suppressed TC activity over lower latitudes, opposite to that during JAS(0) (cf. Figs. 12c,k).

These two types of seasonal control of ENSO on TC activity are largely reproduced by HiRAM despite some systematic biases in the anomaly of TC track density (Figs. 13 and 14). Some significant discrepancies need to be noted. First, for both modes, particularly the first one, the center of the associated SST anomalies over the tropical Pacific shifts westward. This is probably due to the bias in the sensitivity of atmospheric circulation in the model to prescribed SSTs. Second, for the first mode, the modeled TC track density responses not only to the equatorial Pacific SST anomalies but also even more strongly to changes in SSTs over the off-equatorial tropical central North Pacific (Fig. 13). The importance of the SST anomaly over the latter region in determining the East Asian TC activity has recently been emphasized by Jin et al. (2013). In observations, however, SST anomalies over the equatorial regions appear to be more important, except during AMJ(0) (Fig. 11). Thus, more effort is needed in identifying and understanding the areas over which the SST anomalies are more critical in affecting the WNP TC activity.

In addition, we note that the cumulative effect of these two types of ENSO during their developing phase [i.e., from AMJ(0) through OND(0)] is generally consistent with the two modes of annual TC track density discussed in section 3b.[5] It is also interesting to note that among the three seasons when TC activity is most active (i.e., AMJ, JAS, and OND), AMJ appears to be the one where the model response is the strongest (Figs. 13a and 14a). In contrast, in the other two seasons, particularly during JAS (Figs. 13b and 14b), the SST control on TC activity is relatively weak. This is very likely related to the seasonal dependence of the internal variability, which we will discuss in the next section.

4. Internal variability

While the TC track density responds to prescribed SSTs, it also exhibits certain randomness owing to the chaotic nature of the atmospheric processes. In this section, we attempt to identify areas and seasons in which the internal variability is large, and to assess the potential predictability of local TC occurrence.

We use the signal-to-noise ratio (SNR) to measure the amplitude of internal variability (Mei et al. 2014):

$$R = \frac{\sigma_F}{\sigma_I}, \tag{1}$$

where σ_F is the standard deviation of the ensemble mean component (i.e., the forced response), and σ_I represents internal variability and is the standard deviation of the departures from the ensemble mean in all three member runs. A large value of R suggests weak internal variability and thus high potential predictability. Figure 15a shows the calculated SNR of the HiRAM-simulated annual TC track density. Values exceeding 1 can be found over the main development region (MDR) of the WNP TCs, whereas small values are primarily along the East and South Asian coastal regions, particularly over the northern SCS, indicating a low predictability of TC landfall.

Wu et al. (2012) recently find that TC detection algorithm can contribute to the large internal variability in TC activity since TCs detected in models need to satisfy several

[5] In observations, the hybrid CP and EP ENSO and the conventional EP ENSO during their developing phase [i.e., from AMJ(0) through OND(0)] have a similar annual cumulative effect on the anomalous spatial pattern of TC track density (i.e., a nearly-basin-wide pattern). This explains why the observed annual TC track density shows only one EOF mode on interannual timescales rather than two modes as the HiRAM simulations.

criteria. They also show that TC frequency in model simulations is sensitive to intensity criteria. Because TC intensity changes considerably near the coastal regions, the sensitivity is expected to be amplified there. To understand whether the large internal variability in TC track density along the costal regions is due to the TC detection algorithm, we repeated the calculation of the SNR using TCs detected and tracked based on various detection schemes that differ in the minimum value of one or more of following metrics: maximum 850-hPa relative vorticity, maximum temperature anomaly averaged between 300 and 500 hPa, maximum surface wind speed, and track duration (criteria of other aspects, such as SLP, are the same as described in Appendix A). We find the results are most sensitive to the duration (not shown), consistent with Wu et al. (2012). Without a limit on duration, the SNR increases over most of the area south of 30°N. But for all the TC detection schemes, the internal variability along the coastal regions is always large. We further examined the spatial distribution of climatological TC lysis detected based on the scheme described in Appendix A. We find only few TCs disappear over the ocean within 800 km of the coasts, and many TCs can make landfall. This suggests that changes in TC intensity near the coastal area are not the primary reason for the large internal variability near the East Asian coastal regions.

Instead, we suspect the large internal variability along the coastal regions and small variability in the MDR may be related to the fact that TCs prefer a westward-to-northwestward movement in the MDR while the tracks are very diverse on intraseasonal timescales west of the MDR (e.g., Camargo et al. 2007a); the SNR of TC genesis over the TC MDR is above 1 only over a small portion of this region and thus makes a small, if any, contribution to the weak internal variability of TC track density in the MDR. A further exploration of the connection between the internal variability of TC track density and the variability in atmospheric environmental conditions is left for a future study.

As discussed in section 3c, the forced response appears to be stronger during AMJ than during JAS and OND. Here we examine the seasonal dependence of internal variability. Figures 15b,c,d display the SNR for TC track density for the early (AMJ), peak (JAS), and late (OND) TC seasons. It is clear that the randomness in TC track density is relatively weak during AMJ when TC activity is also relatively weak, whereas the internal variability exceeds the forced response during JAS when TCs are most active. It is worth mentioning that of the four months (i.e., July-October) considered, Wu et al. (2012) find strong month-to-month variations of internal variability in WNP TC counts with the largest internal variability in August. In addition, we note that in all seasons the TC track density along the coast of

East and Southeast Asia, especially over the northern SCS, is quite chaotic.

Previous studies on regional climate modeling suggest that downscaling can significantly diminish the inherent internal variability because of the constraints on lateral boundary conditions, and that a smaller model domain generally leads to weaker internal variability (e.g., Caya and Biner 2004; Alexandru et al. 2007). To examine whether this also holds for the simulation of TC track density, we use an ensemble of four members of downscaling simulated WNP TCs from iRAM. Figure 15e shows the calculated SNR of TC track density during the peak TC season. Indeed, the internal variability is much weaker in the regional than global model, with the SNR in iRAM over much of the WNP greater than 1 (Fig. 15e). In spite of the advantages of regional downscaling simulations in suppressing the internal variability, however, the SNR of TC track density is still quite small over the northern SCS and along the coasts of East Asia (Fig. 15e), which is generally consistent with the conclusions from HiRAM simulations.

Mei et al. (2014) suggest that in the NA, basin-integrated metrics, such as the basin-wide total TC counts/days, exhibit weaker internal variability and thus are generally more predictable than local TC occurrence, particularly along the coasts. To examine whether this also holds true for the WNP, we computed the SNR for both the total TC days and TC counts of the whole year as well as of individual seasons (Table 1). For all seasons considered, the SNR of basin-integrated metrics is larger than that of local TC track density over most of the WNP. The internal variability in basin total TC days and counts also has strong seasonal variations: it is weakest in the early TC season and strongest in the peak TC season. This feature is consistent with the seasonal dependence of TC track density. We conclude that as in the NA, in the WNP basin-integrated measures are more predictable than local TC occurrence, and TC activity over the peak TC season shows the strongest randomness, posing a serious challenge for the prediction as well as projection of TC threats to human society.

5. Summary and Conclusions

We have examined the SST-forced variability in tropical cyclone (TC) track density over the western North Pacific (WNP) between 1979 and 2008 using TC tracks from both observations and simulations based on a 25-km-resolution GFDL High-Resolution Atmospheric Model (HiRAM). The model is forced by observed sea surface temperatures (SSTs), and is able to capture the observed variability of annual WNP TC counts, particularly on low-frequency timescales. HiRAM also generally reproduces the observed spatial distribution of climatological WNP TC track density, despite an underestimation over the South China Sea (SCS).

The forced variability of TC track density is studied separately on decadal and interannual timescales with the leading modes extracted by means of an empirical orthogonal function (EOF) analysis. The decadal variability is shown to be dominated by two modes in both observations and HiRAM simulations: a nearly-basin-wide mode, and a dipole mode between the subtropics and lower latitudes. The former mode, with the TC activity peaking in early 1990s, is closely related to variations in WNP TC counts. This mode is primarily driven by low-frequency variations in SSTs over the off-equatorial tropical central North Pacific: anomalously high SSTs there reduce sea level pressure (SLP), increase low-level vorticity, and enhance mid-level upward motion over the WNP, and thereby produce above-normal TC counts and track density in the WNP. The second mode exhibits a phase shift around the mid-1990s, and might be in association with the Atlantic Multidecadal Oscillation. This mode, however, appears not as robust as the first mode, and needs longer model simulations and further exploration.

On interannual timescales, the HiRAM-simulated TC track density is also controlled by two modes. The first mode features a basin-wide mode, and is linked to interannual variations in annual TC number. Analyses of SSTs and atmospheric circulation reveal that a positive phase of this mode can be attributed to above-normal SSTs over the equatorial and northern off-equatorial tropical central Pacific and/or below-normal SSTs over the eastern tropical Indian Ocean, and might be connected to the central Pacific (CP) El Niño. These anomalous SSTs tend to reduce the WNP SLP, increase low-level vorticity, and enhance mid-level upward motion, and thus produce favorable conditions for the WNP TC activity. The other leading mode is characterized by a southwest-northeast dipole in TC track density, mirroring a classical pattern induced by the conventional ENSO. During a conventional El Niño event, a meridional wave train is generated over the WNP, with the southeastern quadrant of the WNP experiencing a favorable atmospheric environment similar to that of the first leading mode and the northwestern quadrant experiencing unfavorable conditions.

In observations, however, the interannual variability of the WNP TC track density is dominated by only one physically meaningful EOF mode, featuring a pattern that TC activity over the open ocean varies homogeneously and in an opposite manner to that over the southern SCS and along the coasts of China. This mode can be viewed as a combination of the two leading modes described above from HiRAM simulations, because a linear combination of their principal components (PCs) highly correlates with the PC of the sole leading mode in observations. This indicates that in reality the CP-type of ENSO may not be distinct from the conventional eastern Pacific (EP) ENSO in modulating the *annually integrated* TC track density over the WNP.

We have further examined the seasonality of the WNP TC track density variability based on a joint EOF analysis over consecutive seasons extending from April-May-June (AMJ) of the first year to AMJ of the following year. In observations, the seasonal evolution of the anomalous pattern in TC track density is modulated by two types of ENSO: a hybrid CP and EP ENSO, and a conventional EP ENSO. These two kinds of ENSO differ in various aspects, including amplitude and location of the maximum SST anomaly in the tropical Pacific, and pace of the decay. The accompanied evolution of anomalous SST pattern in the Indian Ocean also shows remarkable differences. These, as expected, induce distinct responses in the atmospheric circulation, and thereby lead to pronounced differences in the spatial distribution and seasonal evolution of TC track density.

The HiRAM simulations show similar results. But the underlying SST anomalies are located slightly to the west of these in observations, indicating the difference between the model and observations in the sensitivity of the response to SST anomalies in various regions. In addition, we note that the cumulative effect of the two types of ENSO during their developing phase [i.e., from AMJ(0) to OND(0)] is generally consistent with the two modes of annual TC track density.

The signal-to-noise ratio (SNR), defined as the ratio of the standard deviation of the ensemble mean to that of the deviations of the three members from the ensemble mean, is computed to characterize the internal variability. The SNR of the TC track density is found to be large over the TC main development region and is very small in the SCS and along the coast of East Asia for both annual and seasonal statistics. This spatial inhomogeneity in SNR of the track density shows weak dependence on TC detection algorithm, and is mostly related to the internal variability in TC tracks. The internal variability in tracks, in turn, may be related to the intraseasonal variability in the WNP atmospheric circulation (such as monsoon trough and subtropical high; e.g., Chen et al. 2009; Wu et al. 2011; Li and Zhou 2013), an issue that needs further exploration. The randomness in simulated TC track density is also found to be larger during the peak and late TC seasons (i.e., JAS and

OND, respectively) than in the early season (i.e., AMJ). This suggests that TC track density, particularly that related to landfall, is less predictable during TC-active seasons, highlighting challenges for seasonal TC prediction, especially for landfall TCs. Downscaling using the IPRC Regional Atmospheric Model (iRAM) greatly reduces the internal variability of TC track density, but the SNR over the northern SCS and along the coastal regions of East Asia remains low. For both models (i.e., HiRAM and iRAM) basin-integrated metrics are more predictable than local TC occurrence.

Acknowledgments.

This work was supported by NSF Grant AGS-1305719 and NOAA Grant NA13OAR4310092. We thank Prof. Kerry Emanuel for sharing the compiled tropical cyclone best track data. Y. Wang thanks Prof. Chun-Chieh Wu and Dr. Ruifen Zhan for making the iRAM TC track data available for this study.

APPENDIX A

Tropical Cyclone Detection and Tracking in HiRAM

The algorithm of detecting and tracking TCs in HiRAM is originally described in Mei et al. (2014), and is presented here for the convenience of reference. It uses 6-hr atmospheric fields including near-surface winds, SLP, 850-hPa vorticity, and 300-500 hPa averaged temperature to detect and track TCs following the methodology modified from Knutson et al. (2007) and Zhao et al. (2009). Specifically, potential storms are first identified using the following criteria:

(1) The maximum of 850-hPa relative vorticity exceeds 3.2×10^{-4} s^{-1}.

(2) The local minimum in SLP, which must be within a distance of 2° latitude or longitude from the maximum in 850-hPa relative vorticity, is defined as the storm center and is at least 6 hPa lower than the environment. The local maximum surface (represented as the lowest model level) wind speed within an area of 2.6° latitude and 2.6° longitude is detected to represent the storm intensity.

(3) The local maximum of the temperature averaged between 300 and 500 hPa is defined as the center of the storm warm core. Its distance from the storm center must be within 2° latitude or longitude, and its temperature must be at least 1°C warmer than the environment.

After identifying all the potential storm snapshots, a trajectory analysis is then performed to find the storm tracks. The qualified tracks must meet the following two conditions:

(1) The distance between two consecutive snapshots (with a time interval of 6 hr) must be shorter than 400 km.

(2) The track must be longer than 4 days, and the maximum surface wind speed is greater than 17.5 m s^{-1} during the TC life cycle.

APPENDIX B

Downscaling iRAM Simulations and Associated Tropical Cyclone Detection and Tracking

The iRAM simulations and associated algorithm of TC detecting and tracking are originally described in Wu et al. (2012), and are presented here for the convenience of reference. The model domain in use extends from 20°S to 59.8°N and from 100°E to 160°W, covering the South China Sea and the WNP, with a horizontal resolution of 0.2°. There are 28 levels in the vertical with relatively higher resolutions in the planetary boundary layer, and the lowest level is about 35 m above the surface. The model initial and lateral boundary conditions are obtained from the NCEP/NCAR reanalysis 1 (Kalnay et al. 1996). SSTs are constructed using the Reynolds weekly SST data (Reynolds et al. 2002). Totally there are four simulations. They have the same lateral boundary conditions for the atmospheric fields and the same prescribed SSTs, and are only different in initial conditions.

The model TCs are detected and tracked using 6-hr model outputs and using a method modified from Nguyen and Walsh (2001) and Stowasser et al. (2007). The detailed criteria are listed below:

(1) The local maximum in the 850-hPa relative vorticity must exceed 5×10^{-5} s^{-1}.

(2) The local minimum in SLP must be located within a distance of 4° latitude or longitude from the maximum in the 850-hPa relative vorticity, and the location of this minimum in SLP is defined as the storm center.

(3) The azimuthally-mean tangential wind speed at 850 hPa must be higher than that at 300 hPa.

(4) The nearest local maximum in 200-500 hPa averaged temperature is distinguishable. Its location, defined as the center of the warm core, must be within a distance of 2.5° latitude or longitude from the storm center. The temperature of the warm core must be at least 0.5°C warmer than the environment in all directions within a distance of 7.5° latitude or longitude.

(5) The storm must form south of 35°N.

Then a trajectory analysis is performed to find the TC tracks, which must meet the following two conditions. First, the distance between two consecutive snapshots (with a time interval of 6 hr) must be shorter than 300 km if south of 25°N or shorter than 600 km if north of 25°N. Second, the storm must last at least 2 days and the maximum wind speed at the surface (i.e., the lowest model level) must be greater than 17 m s^{-1} for at least 2 days (not necessarily to be consecutive).

REFERENCES

Aiyyer, A. and C. Thorncroft, 2011: Interannual-to-multidecadal variability of vertical shear and tropical cyclone activity. *J. Climate*, **24**, 2949–2962.

Alexandru, A., R. de Elia, and R. Laprise, 2007: Internal variability in regional climate downscaling at the seasonal scale. *Mon. Wea. Rev.*, **135**, 3221–3238.

Annamalai, H., S.-P. Xie, J. P. McCreary, and R. Murtugudde, 2005: Impact of Indian Ocean sea surface temperature on developing El Nino. *J. Climate*, **18**, 302–319.

Ashok, K., S. K. Behera, S. A. Rao, H. Weng, and T. Yamagata, 2007: El Nino Modoki and its possible teleconnection. *J. Geophys. Res.*, **112**, C11007, doi:10.1029/2006JC003798.

Camargo, S. J., A. W. Robertson, S. J. Gaffney, P. Smyth, and M. Ghil, 2007a: Cluster analysis of typhoon tracks. Part I: General properties. *J. Climate*, **20**, 3635–3653.

Camargo, S. J., A. W. Robertson, S. J. Gaffney, P. Smyth, and M. Ghil, 2007b: Cluster analysis of typhoon tracks. Part II: Large-scale circulation and ENSO. *J. Climate*, **20**, 3654–3676.

Camargo, S. J. and A. H. Sobel, 2005: Western North Pacific tropical cyclone intensity and ENSO. *J. Climate*, **18 (15)**, 2996–3006.

Caya, D. and S. Biner, 2004: Internal variability of RCM simulations over an annual cycle. *Climate Dyn.*, **22**, 33–46.

Chan, J. C. L., 1985: Tropical cyclone activity in the northwest Pacific in relation to the El Nino/Southern Oscillation phenomenon. *Mon. Wea. Rev.*, **113**, 599–606.

Chan, J. C. L. and J. Shi, 1996: Long-term trends and interannual variability in tropical cyclone activity over the western North Pacific. *Geophy. Res. Lett.*, **23 (20)**, 2765–2767.

Chen, T.-C., S.-Y. Wang, M.-C. Yen, and A. J. Clark, 2009: Impact of the intraseasonal variability of the western North Pacific large-scale circulation on tropical cyclone tracks. *Weather Forecast.*, **24**, 646–666.

Chia, H. H. and C. F. Ropelewski, 2002: The interannual variability in the genesis location of tropical cyclones in the northwest Pacific. *J. Climate*, **15**, 2934–2944.

Chu, J.-H., C. R. Sampson, A. S. Levine, and E. Fukada, 2002: The Joint Typhoon Warning Center tropical cyclone best-tracks, 1945-2000. Tech. Rep. Ref. NRL/MR/7540-02-16, Nav. Res. Lab., Washington, DC, USA. Available at `http://www.usno.navy.mil/NOOC/nmfc-ph/RSS/jtwc/best_tracks/`.

Du, Y., S.-P. Xie, G. Huang, and K. Hu, 2009: Role of air-sea interaction in the long persistence of El Nino-induced North Indian Ocean warming. *J. Climate*, **22**, 2023–2038.

Du, Y., L. Yang, and S.-P. Xie, 2011: Tropical Indian Ocean influence on Northwest Pacific tropical cyclones in summer following strong El Nino. *J. Climate*, **24**, 315–322.

Elsner, J. B. and B. Kocher, 2000: Global tropical cyclone activity: A link to the North Atlantic Oscillation. *Geophys. Res. Lett.*, **27 (1)**, 129–132.

Elsner, J. B. and K. B. Liu, 2003: Examining the ENSO-typhoon hopothesis. *Climate Res.*, **25**, 43–54.

Emanuel, K., 2007: Environmental factors affecting tropical cyclone power dissipation. *J. Climate*, **20**, 5497–5509.

Griffies, S. M. and K. Bryan, 1997: Predictability of North Atlantic multidecadal climate variability. *Science*, **275**, 181–184.

Harzallah, A. and R. Sadourny, 1995: Internal versus SST-forced atmospheric variability as simulated by an atmospheric general circulation model. *J. Climate*, **8**, 474–495.

Ho, C.-H., J.-J. Baik, J.-H. Kim, D.-Y. Gong, and C.-H. Sui, 2004: Interdecadal changes in smmmertime typhoon tracks. *J. Climate*, **17**, 1767–1776.

Huang, P., C. Chou, and R. Huang, 2011: Modulation of tropical intraseasonal oscillation on tropical cyclone geneses in the western North Pacific. *J. Climate*, **24**, 6339–6352.

Jin, C.-S., C.-H. Ho, J.-H. Kim, D.-K. Lee, D.-H. Cha, and S.-W. Yeh, 2013: Critical role of northern off-equatorial sea surface temperature forcing associated with central Pacific El Nino in more frequent tropical cyclone movements toward East Asia. *J. Climate*, **26**, 2534–2545.

Johnson, N. C., 2013: How many ENSO flavors can we distinguish? *J. Climate*, **26**, 4816–4827.

Kalnay, E., et al., 1996: The NCEP/NCAR 40-year reanalysis project. *Bull. Amer. Meteor. Soc.*, **77**, 437–471.

Kao, H.-Y. and J.-Y. Yu, 2009: Contrasting eastern-Pacific and central-Pacific types of ENSO. *J. Climate*, **22**, 615–632.

Kim, H.-M., P. J. Webster, and J. A. Curry, 2011a: Modulation of North Pacific tropical cyclone activity by three phases of ENSO. *J. Climate*, **24**, 1839–1849.

Kim, H.-S., J.-H. Kim, C.-H. Ho, and P.-S. Chu, 2011b: Pattern classification of typhoon tracks using the fuzzy *c*-means clustering method. *J. Climate*, **24**, 488–508.

Kim, J.-H., C.-H. Ho, and P.-S. Chu, 2010: Dipolar redistribution of summertime tropical cyclone genesis between the Philippine Sea and the northern South China Sea and its possible mechanisms. *J. Geophys. Res.*, **115**, D06104, doi:10.1029/2009JD012196.

Knutson, T. R., J. J. Sirutis, S. T. Garner, I. M. Held, and R. E. Tuleya, 2007: Simulations of the recent multidecadal increase of Atlantic hurricane activity using an 18-km-grid regional model. *Bull. Amer. Meteor. Soc.*, **88**, 1549–1565.

Kosaka, Y., S.-P. Xie, N.-C. Lau, and G. A. Vecchi, 2013: Origin of seasonal predictability for summer climate over the northwestern Pacific. *Proc. Natl. Acad. Sci. U. S. A.*, **110**, 7574–7579.

Kug, J.-S., F.-F. Jin, and S.-I. An, 2009: Two types of El Nino events: Cold tongue El Nino and warm pool El Nino. *J. Climate*, **22**, 1499–1515.

Kug, J.-S. and I.-S. Kang, 2006: Interactive feedback between ENSO and the Indian Ocean. *J. Climate*, **19**, 1784–1801.

Lander, M. A., 1994: An exploratory analysis of the relationship between tropical storm formation in the western North Pacific and ENSO. *Mon. Wea. Rev.*, **122**, 636–651.

Lander, M. A., 1996: Specific tropical cyclone track types and unusual tropical cyclone motions associated with a reverse-oriented monsson trouph in the western North Pacific. *Wea. Forecasting*, **11**, 170–186.

Li, R. C. Y. and W. Zhou, 2013: Modulation of western North Pacific tropical cyclone activity by the ISO. part ii: Tracks and landfalls. *J. Climate*, **26**, 2919–2930.

Liu, K. S. and J. C. L. Chan, 2008: Interdecadal variability of western North Pacific tropical cyclone tracks. *J. Climate*, **21**, 4464–4476.

Liu, K. S. and J. C. L. Chan, 2013: Inactive period of western North Pacific tropical cyclone activity in 1998-2011. *J. Climate*, **26**, 2614–2630.

Matsuura, T., M. Yumoto, and S. Iizuka, 2003: A mechanism of interdecadal variability of tropical cyclone activity over the western North Pacific. *Climate Dyn.*, **21**, 105–117.

Mei, W., S.-P. Xie, and M. Zhao, 2014: Variability of tropical cyclone track density in the North Atlantic: Observations and high-resolution simulations. *J. Climate*, **in press**.

Nguyen, K. C. and K. J. E. Walsh, 2001: Interannual, decadal, and transient greenhouse simulation of tropical cyclone?like vortices in a regional climate model of the South Pacific. *J. Climate*, **14**, 3043–3054.

North, G. R., T. L. Bell, R. F. Cahalan, and F. J. Moeng, 1982: Sampling errors in the estimation of empirical orthogonal functions. *Mon. Weather Rev.*, **110**, 699–706.

Park, D.-S. R., C.-H. Ho, J. H. Kim, and H.-S. Kim, 2013: Spatially inhomogeneous trends of tropical cyclone intensity over the western North Pacific for 1977–2010. *J. Climate*, **26**, 5088–5101.

Rayner, N. A., D. E. Parker, E. B. Horton, C. K. Folland, L. V. Alexander, D. P. Rowell, E. C. Kent, and A. Kaplan, 2003: Global analyses of sea surface temperature, sea ice, and night marine air temperatures since the late nineteen century. *J. Geophys. Res.*, **108**, 4407, doi:10.1029/2002JD002670.

Reynolds, R. W., N. A. Rayner, T. M. Smith, D. C. Stokes, and W. Wang, 2002: An improved in situ and satellite SST analysis for climate. *J. Climate*, **15**, 1609–1625.

Ritchie, A. and G. J. Holland, 1999: Large-scale patterns associated with tropical cyclogenesis in the western Pacific. *Mon. Wea. Rev.*, **127**, 2027–2043.

Stowasser, M., Y. Wang, and K. Hamilton, 2007: Tropical cyclone changes in the western North Pacific in a global warming scenario. *J. Climate*, **20**, 2378–2396.

Tao, L., L. Wu, Y. Wang, and J. Yang, 2012: Influences of tropical Indian Ocean warming and ENSO on tropical cyclone activity over the western North Pacific. *J. Meteor. Soc. Japan*, **90**, 127–144.

Venzke, S., M. R. Allen, R. T. Sutton, and D. P. Powell, 1999: The atmospheric response over the North Atlantic to decadal changes in sea surface temperature. *J. Climate*, **12**, 2562–2584.

Vimont, D. J. and J. P. Kossin, 2007: The Atlantic Meridional Mode and hurricane activity. *Geophys. Res. Lett.*, **34**, L07709, doi:10.1029/2007GL029683.

Wang, B. and J. C. L. Chan, 2002: How strong ENSO events affect tropical storm activity over the western North Pacific. *J. Climate*, **15**, 1643–1658.

Wang, C., C. Li, M. Mu, and W. Duan, 2013: Seasonal modulations of different impacts of two types of ENSO events on tropical cyclone activity in the western North Pacific. *Climate Dyn.*, **40**, 2887–2902.

Watanabe, M. and F.-F. Jin, 2002: Role of Indian Ocean warming in the development of Philippine Sea anticyclone during ENSO. *Geophys. Res. Lett.*, **29**, 1478, doi:10.1029/2001GL014318.

Wu, C.-C., R. Zhan, Y. Lu, and Y. Wang, 2012: Internal variability of the dynamically downscaled tropical cyclone activity over the western North Pacific by the IPRC regional atmospheric model. *J. Climate*, **25**, 2104–2122.

Wu, L., H. Zong, and J. Liang, 2011: Observational analysis of sudden tropical cyclone track changes in the vicinity of the Esat Cnina Sea. *J. Atmos. Sci.*, **68**, 3012–3031.

Wu, M. C., W. L. Chang, and W. M. Leung, 2004: Impacts of El Nino-Southern Oscillation events on tropical cyclone landfalling activity in the western North Pacific. *J. Climate*, **17**, 1419–1428.

Zhan, R., Y. Wang, and X. Lei, 2011a: Contributions of ENSO and East Indian Ocean SSTA to the interannual variability of northwest Pacific tropical cyclone frequency. *J. Climate*, **24**, 509–521.

Zhan, R., Y. Wang, and X. Lei, 2011b: Impact of SSTA in the east Indian Ocean on the frequency of northwest Pacific tropical cyclones: A Regional Atmospheric Model study. *J. Climate*, **24**, 6227–6242.

Zhao, M., I. M. Held, and S.-J. Lin, 2012: Some counter-intuitive dependencies of tropical cyclone frequency on parameters in a GCM. *J. Atmos. Sci.*, **69**, 2272–2283.

Zhao, M., I. M. Held, S.-J. Lin, and G. A. Vecchi, 2009: Simulations of global hurricane climatology, interannual variability, and response to global warming using a 50-km resolution GCM. *J. Climate*, **22**, 6653–6678.

Table 1: SNR for the basin-integrated total TC days and TC counts of the whole year and of individual seasons

	Early TC season (Apr-Jun)	Peak TC season (Jul-Sep)	Late TC season (Oct-Dec)	Whole year (Jan-Dec)
Total TC days	1.65	0.98	1.35	1.68
TC counts	1.62	1.06	1.53	1.71

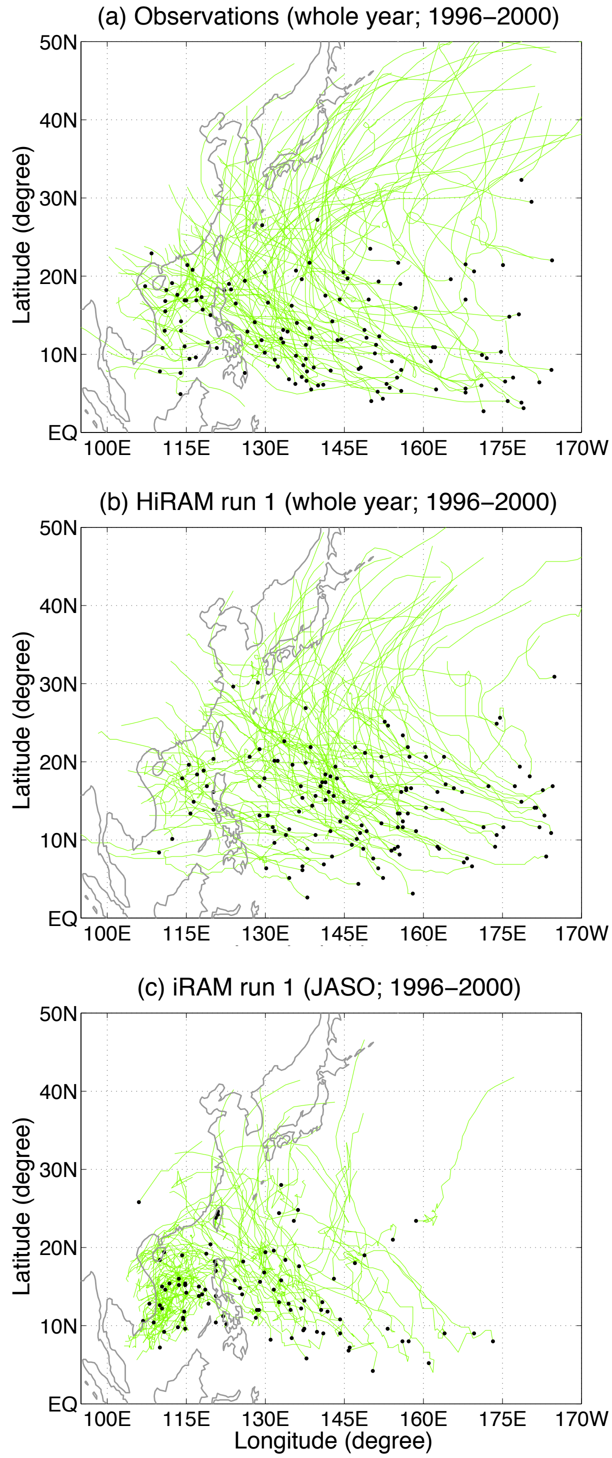

Figure 1: Western North Pacific TC genesis (black dots) and tracks (green curves) of the entire year from observations (a) and one realization of HiRAM (b), and of July–October from one realization of iRAM (c) between 1996 and 2000. Only TCs generated between 100°E and 170°W are shown.

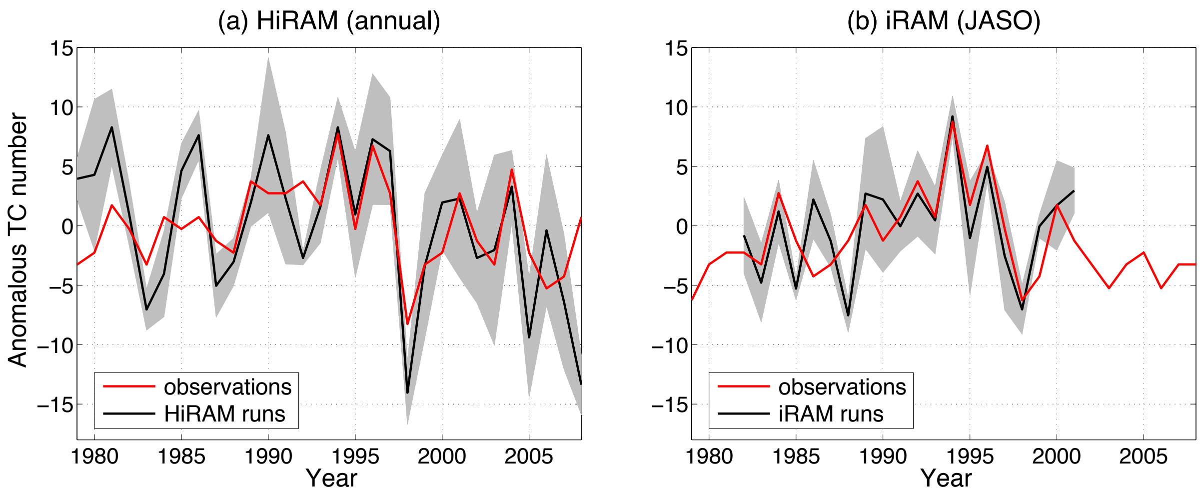

Figure 2: (a) A comparison of observed (red) and HiRAM-simulated (black curve) anomalies in the *annual* number of TCs in the WNP between 1979 and 2008. The climatological mean number is 27.6 and 26.3 respectively in the simulations and observations. The correlation between these two curves is 0.603 ($P = 0.0004$). Gray shading shows the spread of the model results represented as the standard deviations of the results from the three ensemble members. (b) A comparison of observed (red) and iRAM-simulated (black curve) anomalies in the TC number *during July–October*. The climatological mean number between 1982 and 2001 is 19.5 and 19.3 respectively in the simulations and observations. The correlation between these two curves is 0.698 ($P = 0.0006$). Gray shading shows the spread of the model results represented as the standard deviations of the results from the four ensemble members.

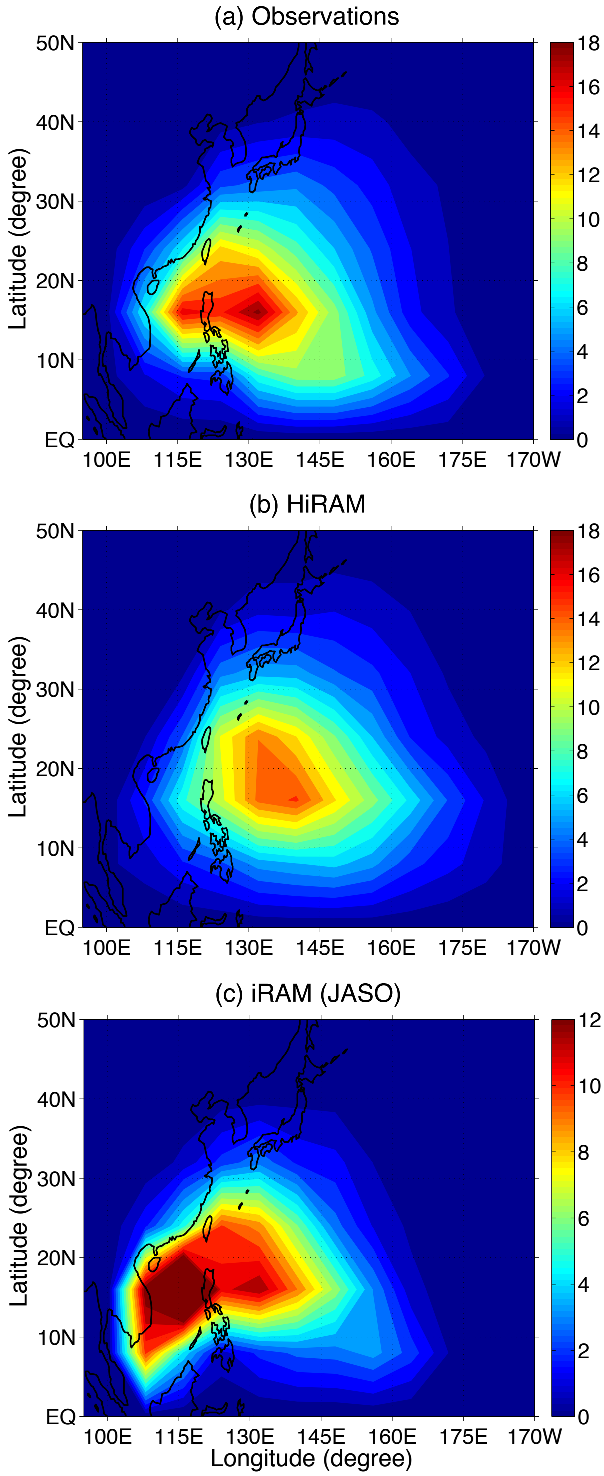

Figure 3: (a) Observed and (b) HiRAM-simulated geographical distribution of the climatological annual TC track density (units: days per year) calculated at each $8^\circ \times 8^\circ$ grid. (c) As in (b), but for iRAM-simulated TC track density during July-October.

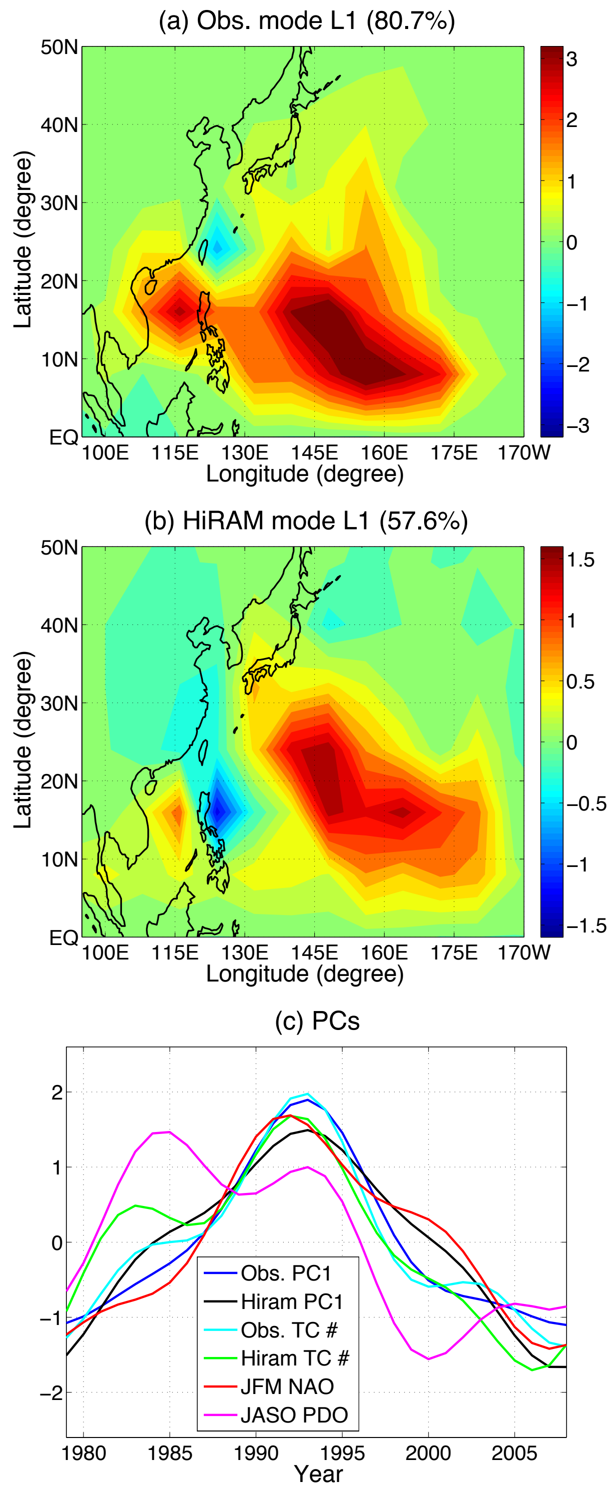

Figure 4: (a) Spatial pattern of the first leading mode of the low-pass-filtered annual TC track density (denoted as mode L1; unit: days per year) in the WNP from observations. (b) As in (a), but for HiRAM-simulated track density. (c) Normalized time series of the corresponding principal component (PC) from observations (blue) and HiRAM simulations (black). Also shown are normalized anomalies of the low-pass-filtered annual TC number in observations (cyan) and HiRAM simulations (green), NAO index of the preceding winter (red), and PDO index of the WNP TC peak season (magenta).

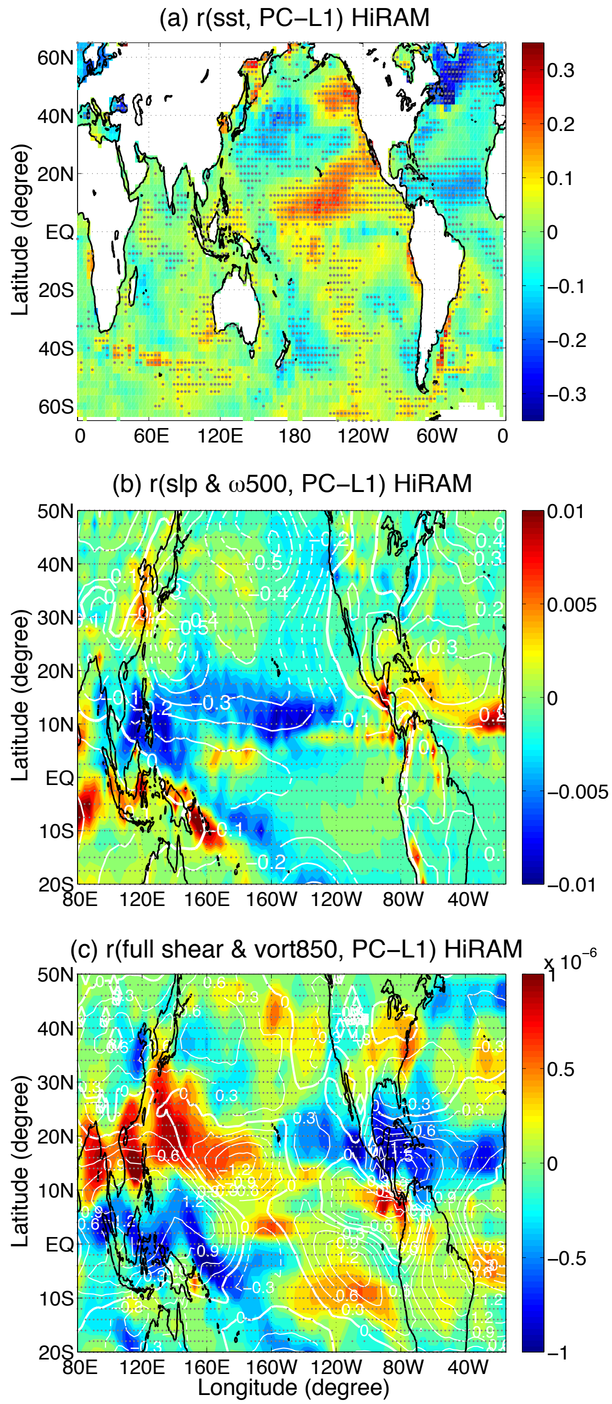

Figure 5: (a) Regression of low-pass-filtered SST anomalies (unit: °C) on the PC of mode L1 from HiRAM simulations shown in Fig. 4c. Stippling indicates linear correlation coefficient exceeding 0.5. (b) As in (a), but for SLP (contours; unit: hPa) and 500-hPa vertical pressure velocity (shading; unit: Pa s^{-1}). (c) As in (a), but for vertical shear of horizontal winds (contours; unit: m s^{-1}) and 850-hPa vorticity (shading; unit: s^{-1}).

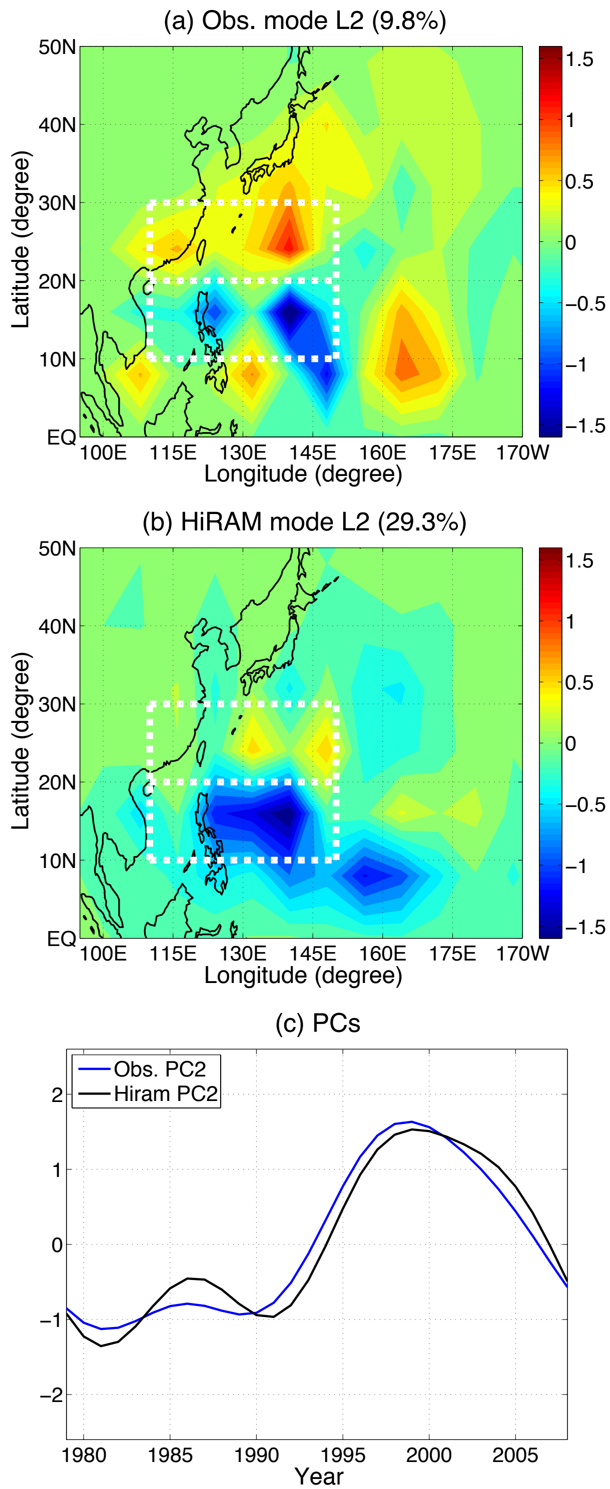

Figure 6: As in Fig. 5, but for the second leading mode (denoted as mode L2) of the low-pass-filterers annual TC track density. Note that although mode L2 in observations only explains 9.8% of the variance, a significance test based on North et al. (1982) suggests that this mode is significant.

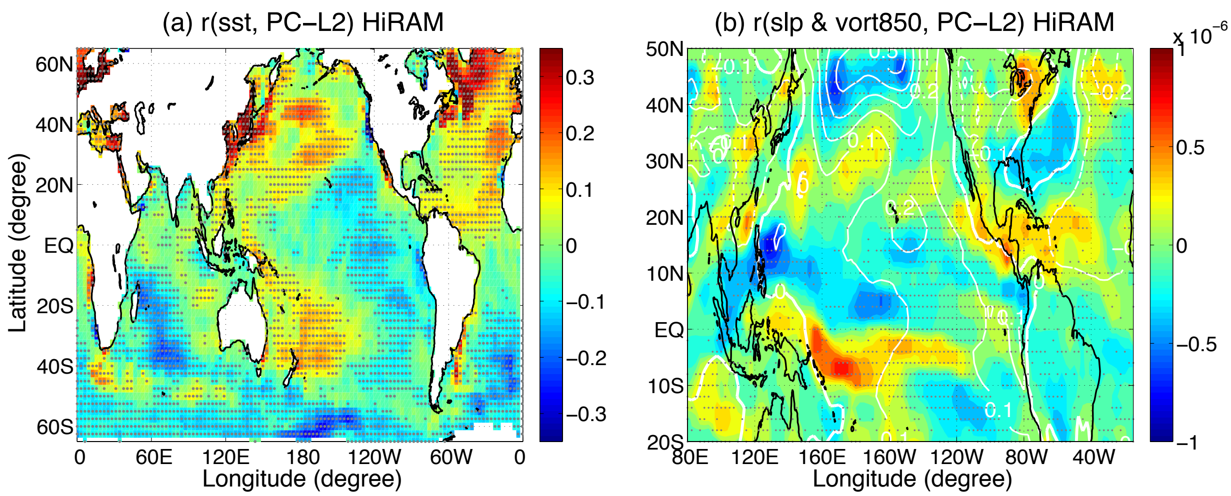

Figure 7: (a) Regression of low-pass-filtered SST anomalies (unit: °C) on the PC of mode L2 from HiRAM simulations shown in Fig. 6c. Stippling indicates linear correlation coefficient exceeding 0.5. (b) As in (a), but for SLP (contours; unit: hPa) and 850-hPa vorticity (shading; unit: s^{-1}).

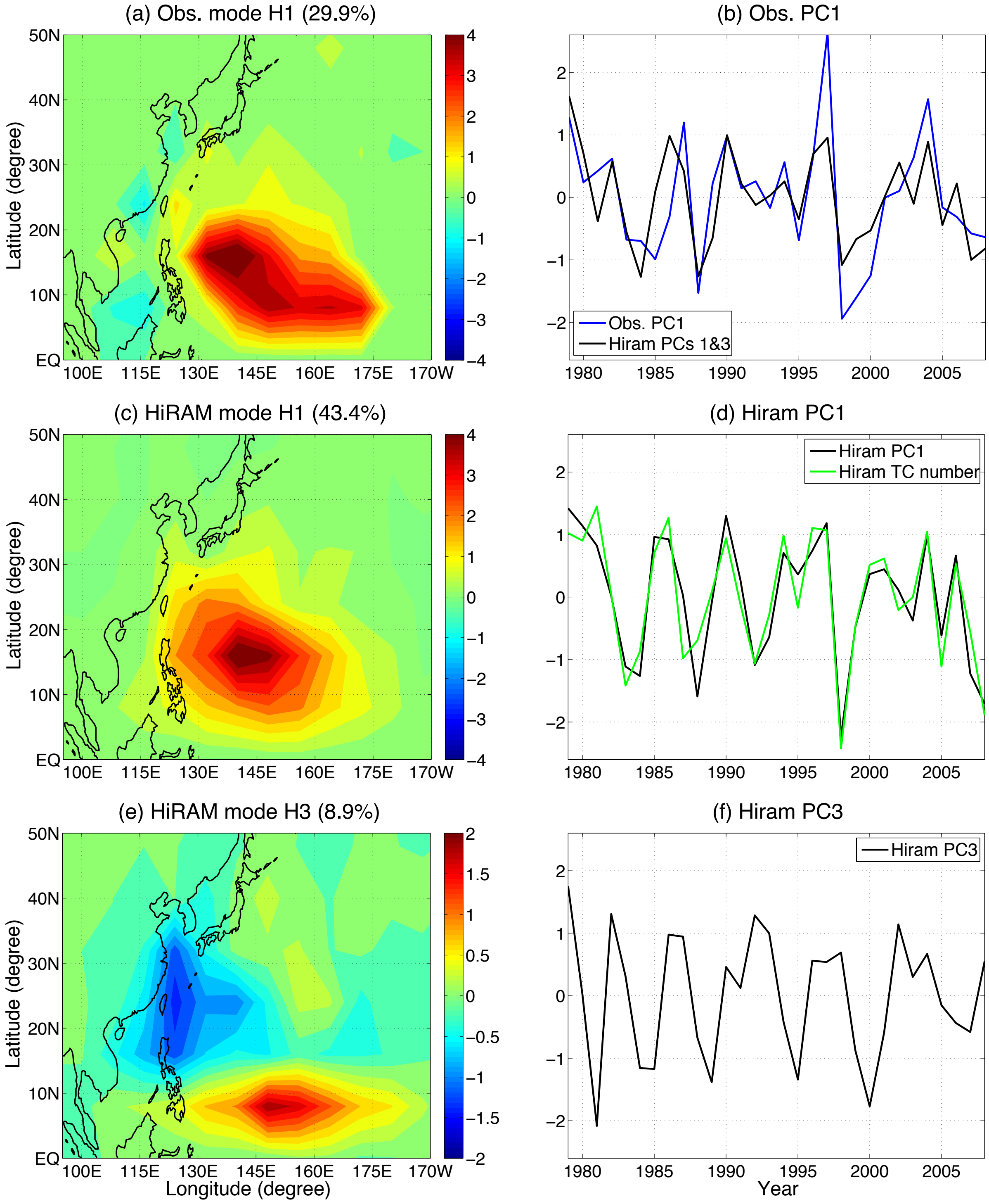

Figure 8: (a) Spatial pattern (unit: days per year) and (b) time series of the PC (blue) for the first leading mode of the high-pass-filtered annual TC track density in observations (denoted as Obs. mode H1). (c) and (d) As in (a) and (b), but for the first leading mode from HiRAM simulations (denoted as HiRAM mode H1). (e) and (f) As in (a) and (b), but for the third leading mode from HiRAM simulations (denoted as HiRAM mode H3). Also shown in (b) is a linear combination of the PCs for modes H1 and H3 from HiRAM simulations (black), and in (d) is the normalized time series of anomalous annual TC counts in HiRAM simulations (green).

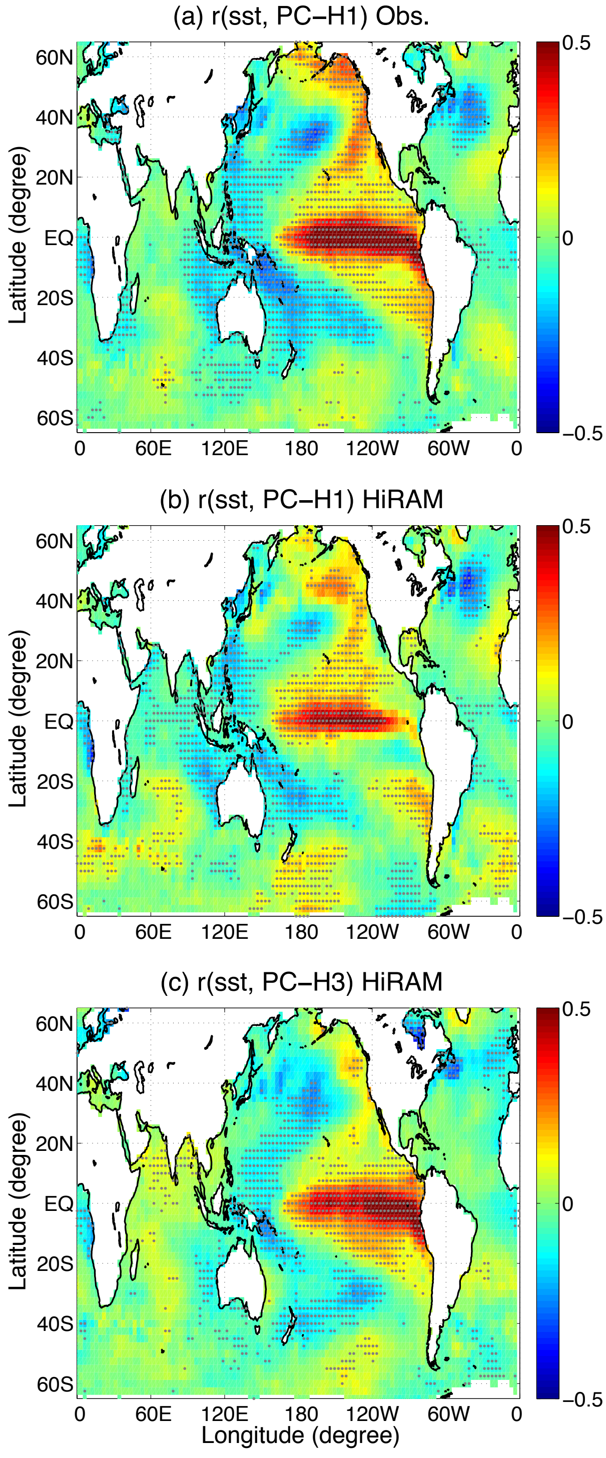

Figure 9: (a) Regression of high-pass-filtered SST anomalies (unit: °C) on the PC of mode H1 from observations shown in Fig. 8a. Stippling indicates linear correlation coefficient at a 0.05 significance level. (b) and (c) As in (a), but respectively for modes H1 and H3 from HiRAM simulations.

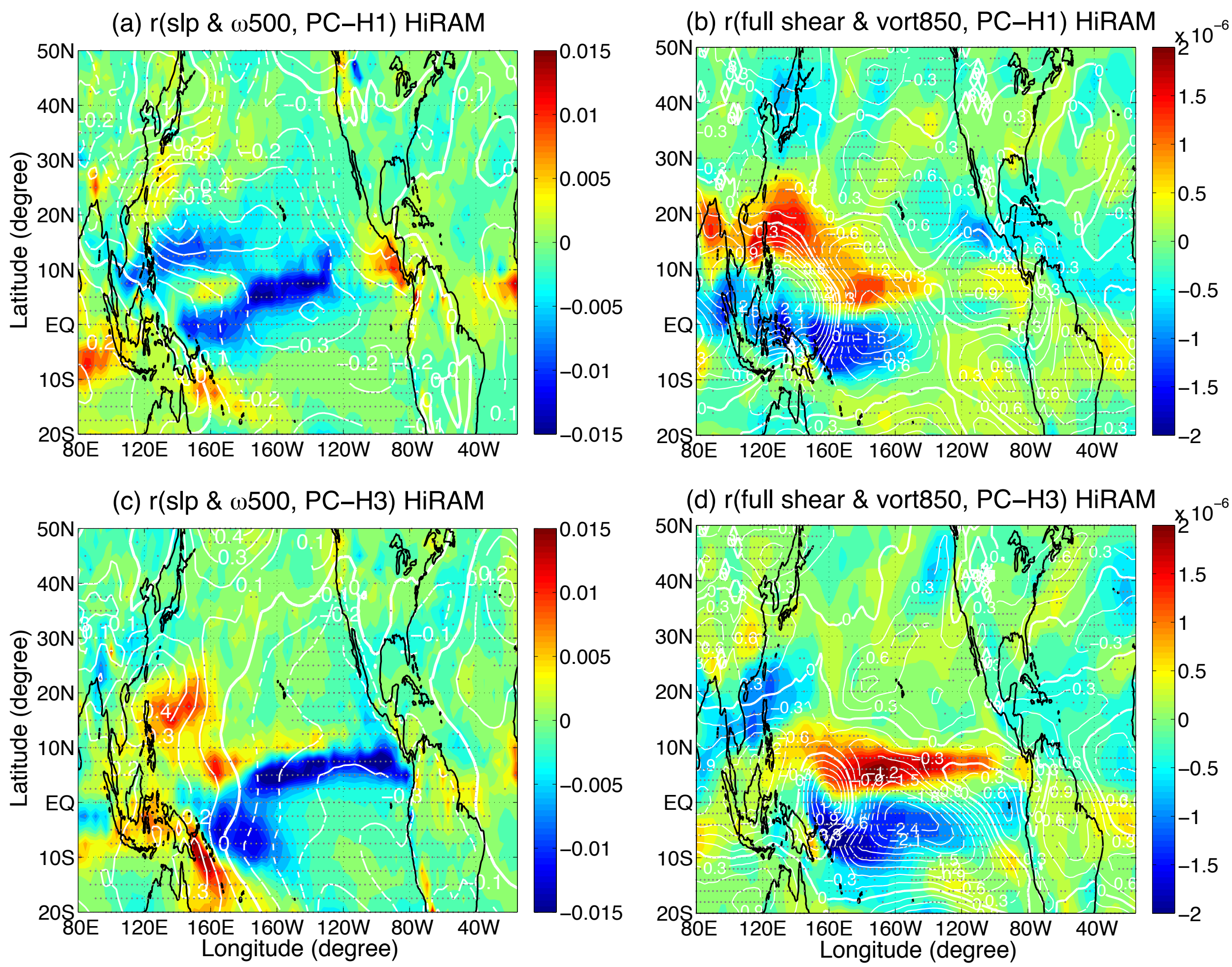

Figure 10: (a) Regression of low-pass-filtered anomalies in SLP (contours; unit: hPa) and 500-hPa vertical pressure velocity (shading; unit: Pa s^{-1}) on the PC of mode H1 from HiRAM simulations shown in Fig. 8d. Stippling indicates linear correlation coefficient at a 0.05 significance level for either SLP or 500-hPa vertical pressure velocity or both. (b) As in (a), but for vertical shear of horizontal winds (contours; unit: m s^{-1}) and 850-hPa vorticity (shading; unit: s^{-1}). (c) and (d) As in (a) and (b), but for mode H3 from HiRAM simulations.

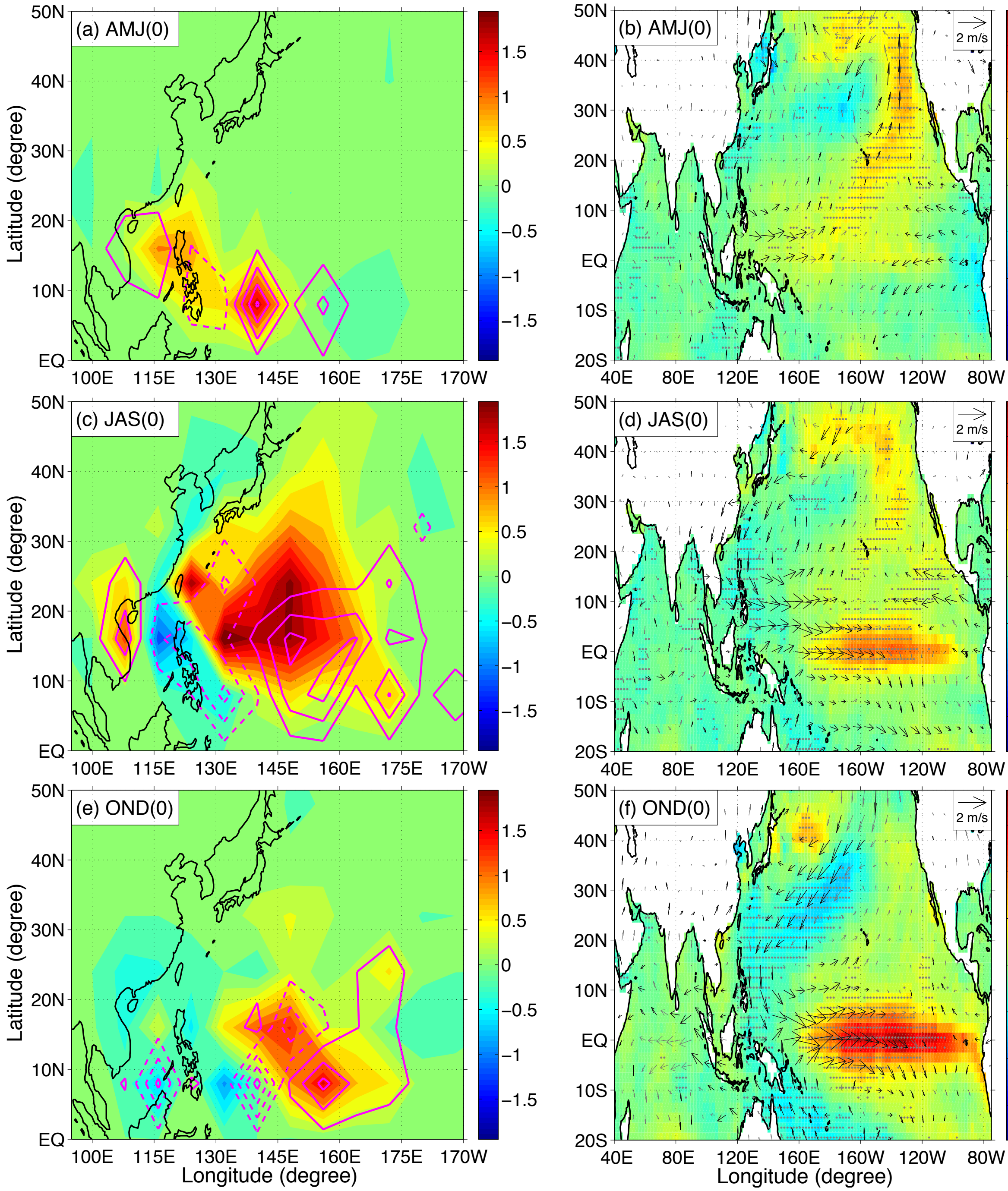

Figure 11: (a)(c)(e)(g)(i) Spatial pattern (shading; unit: days per year) of the first leading mode of the joint EOF analysis of TC track density from AMJ(0) to AMJ(1) in observations (explained variance: 15.1%). Magenta contours show the anomalous pattern of TC genesis regressed on the PC. (b)(d)(f)(h)(j) Anomalous pattern of high-pass-filtered SSTs (shading; unit: °C) and 850-hPa winds (vector; unit: m s^{-1}) regressed on the PC. Stippling indicates linear correlation coefficient at a 0.05 significance level for SSTs, and black arrows for 850-hPa winds. (k)(l) As in (a) and (b), but for regressed patterns for JAS(1).

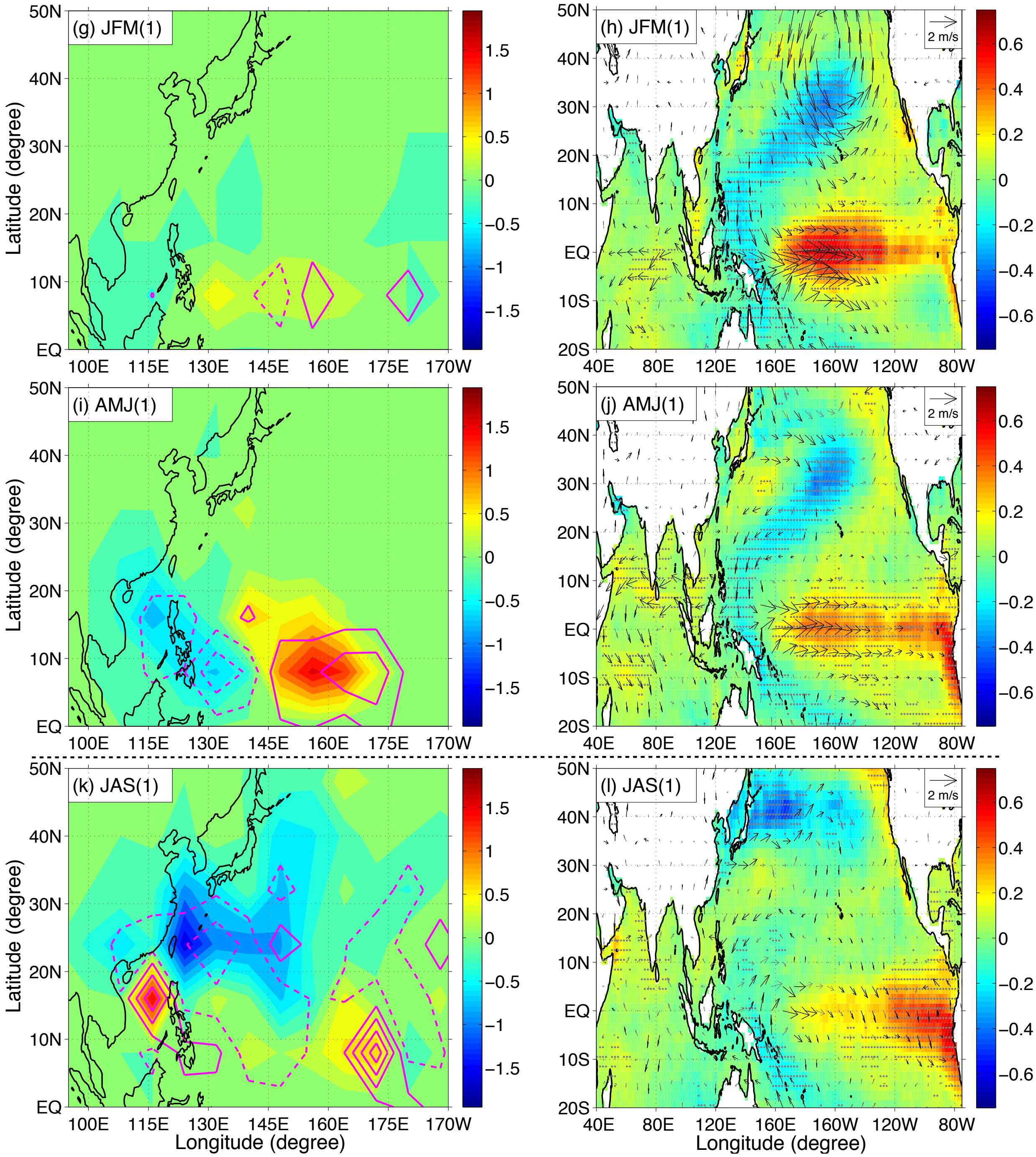

Figure 11: *Continued.*

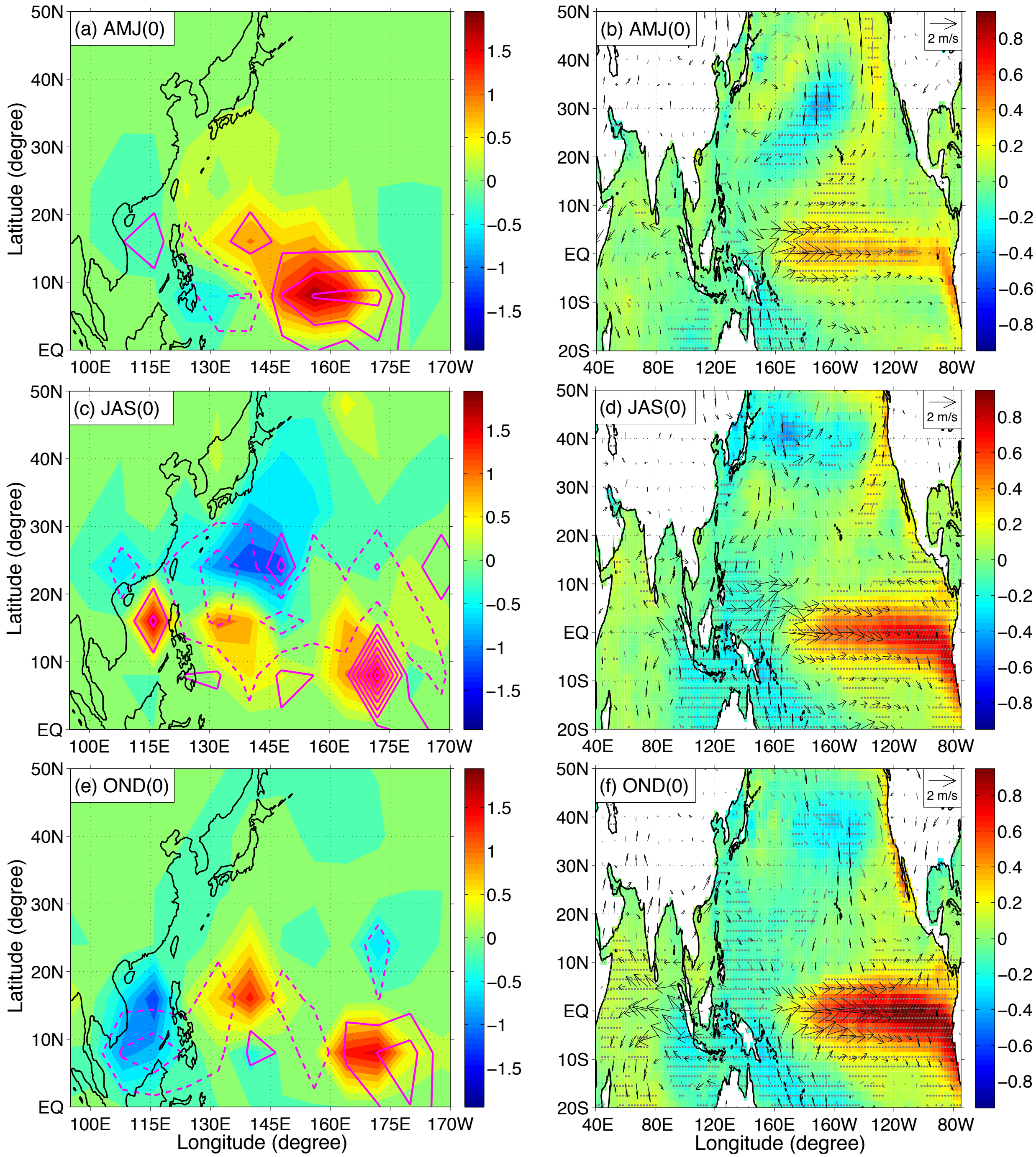

Figure 12: As in Fig. 11, but for the second leading mode from observations (explained variance: 10.8%).

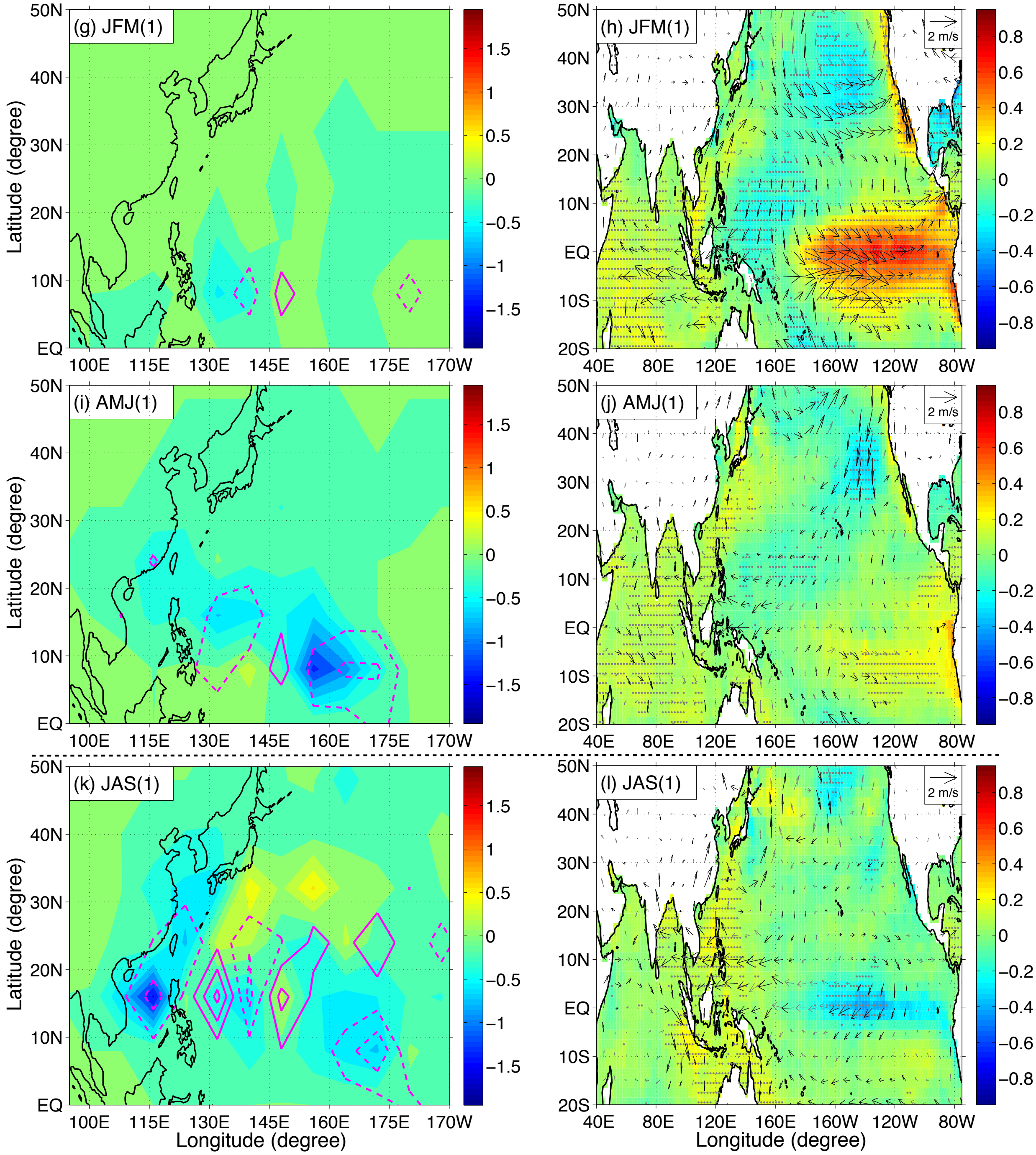

Figure 12: *Continued.*

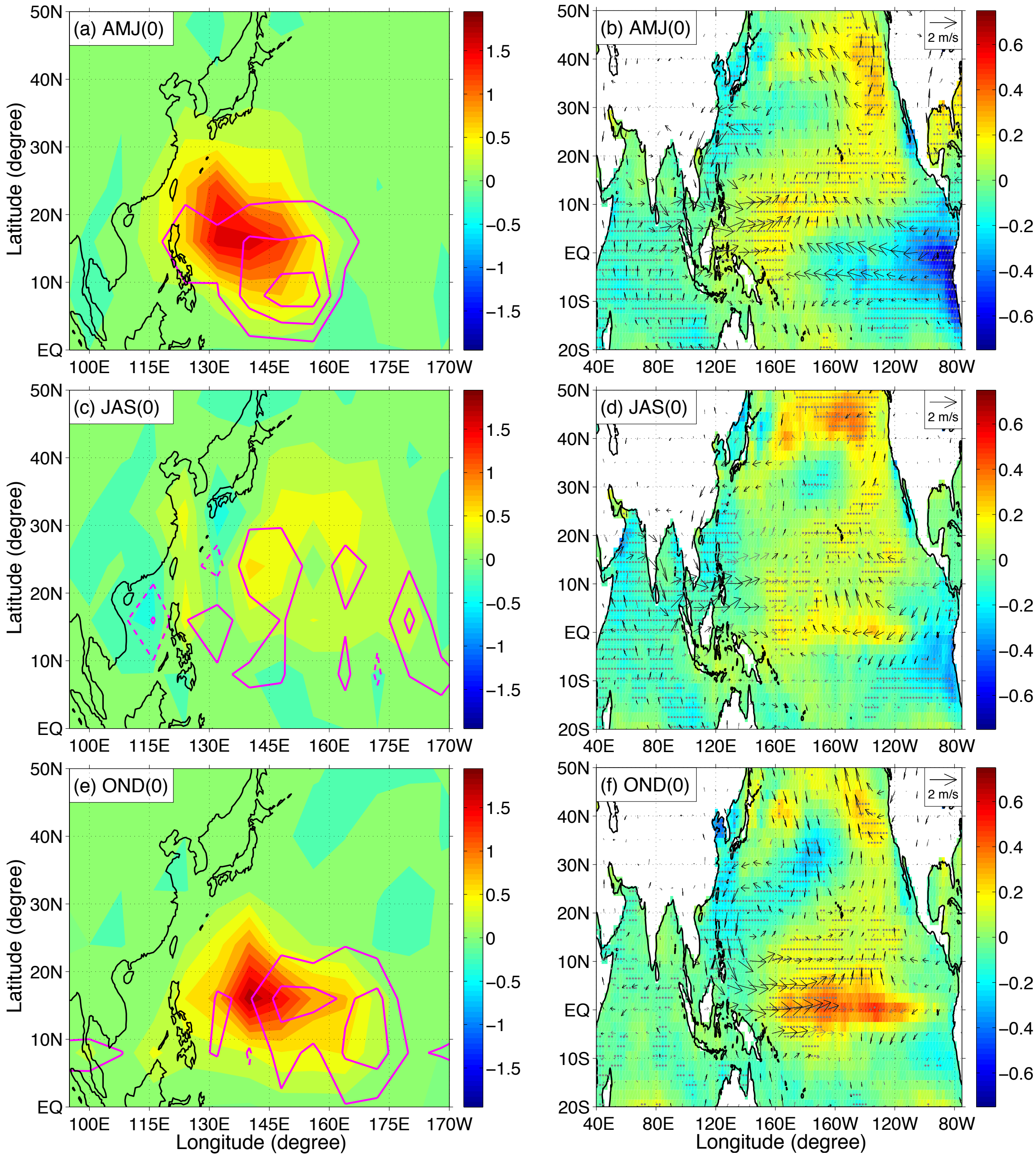

Figure 13: As in Fig. 11, but for the first leading mode from HiRAM simulations (explained variance: 20.0%).

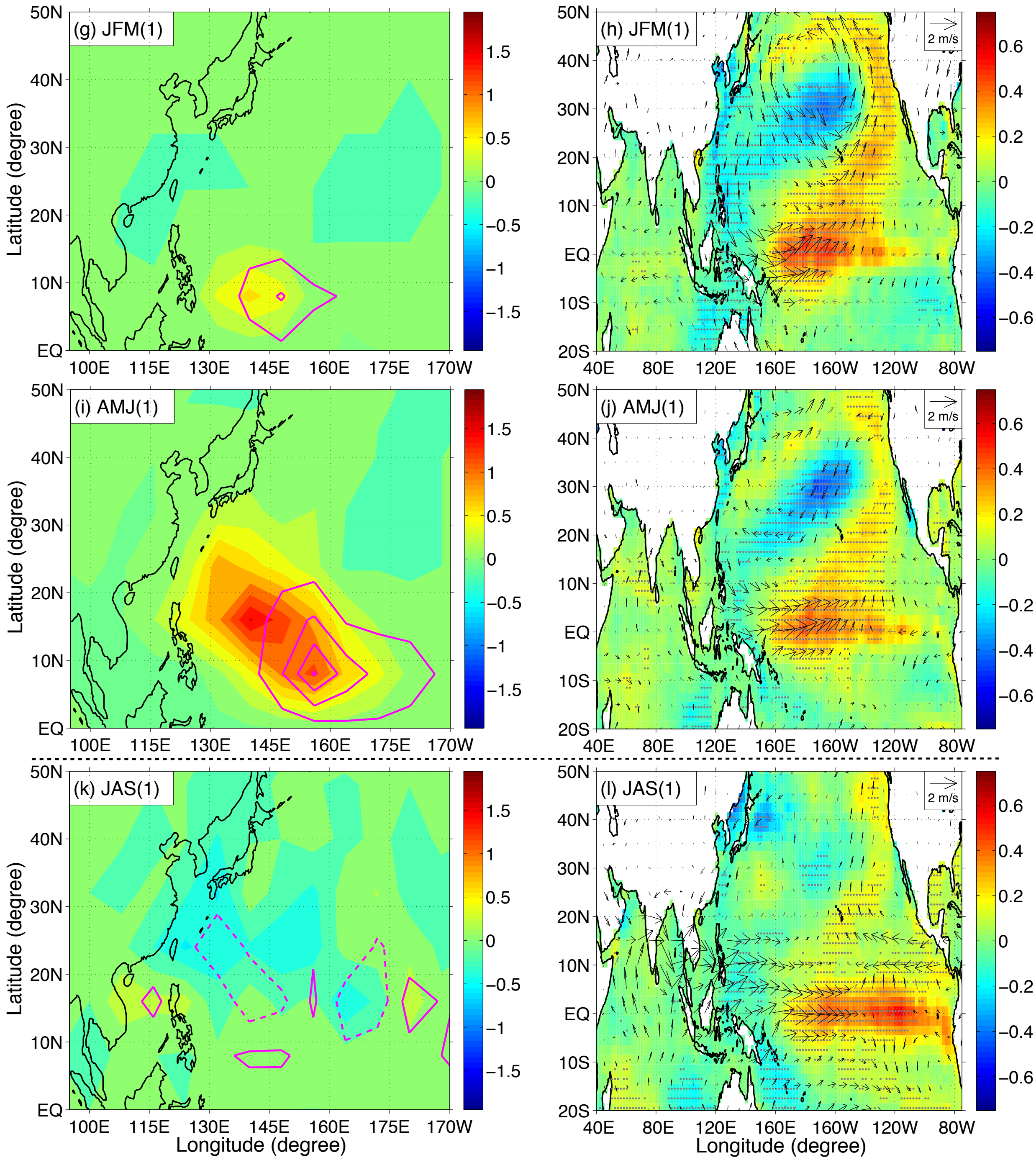

Figure 13: *Continued.*

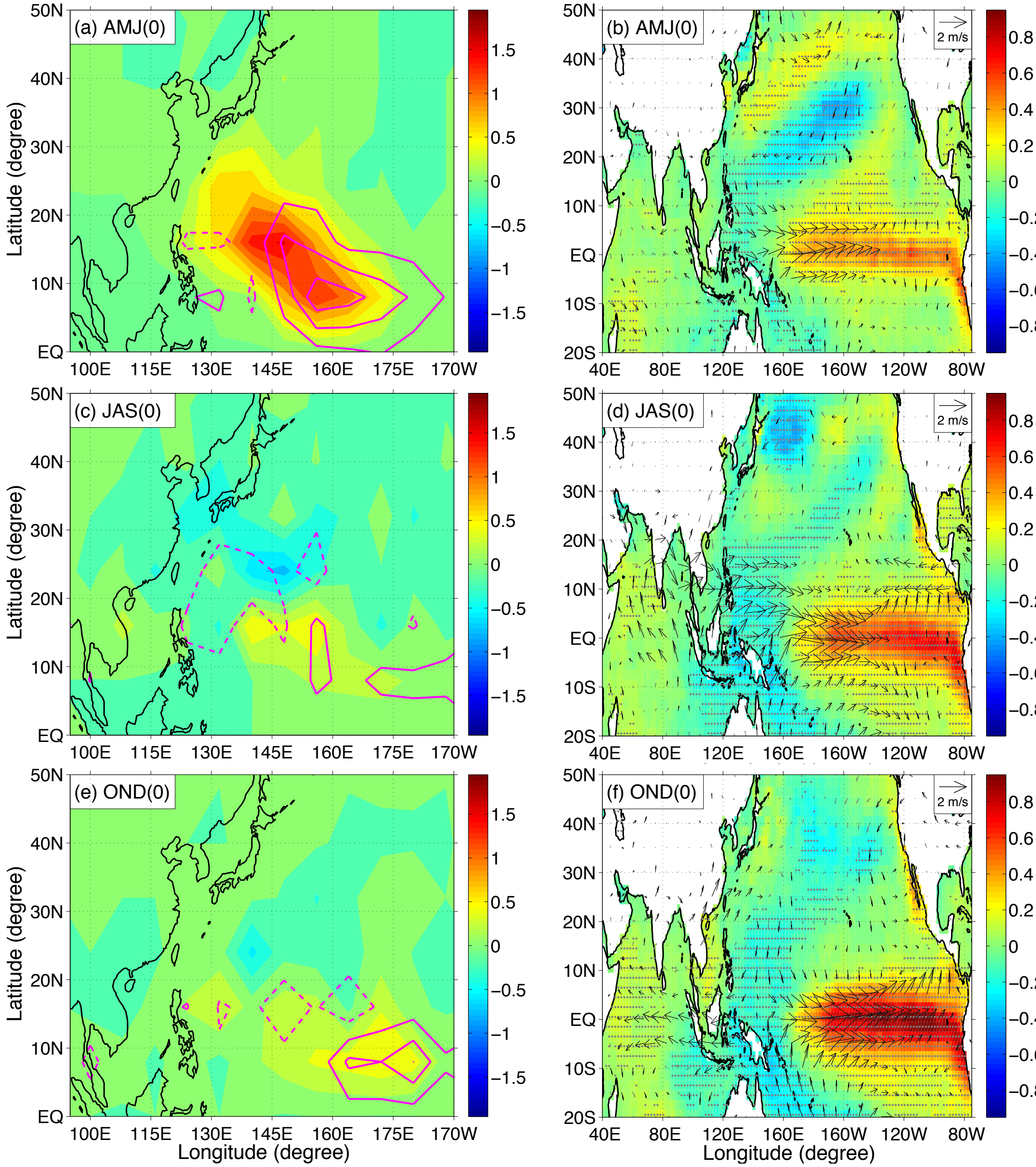

Figure 14: As in Fig. 11, but for the second leading mode from HiRAM simulations (explained variance: 13.8%).

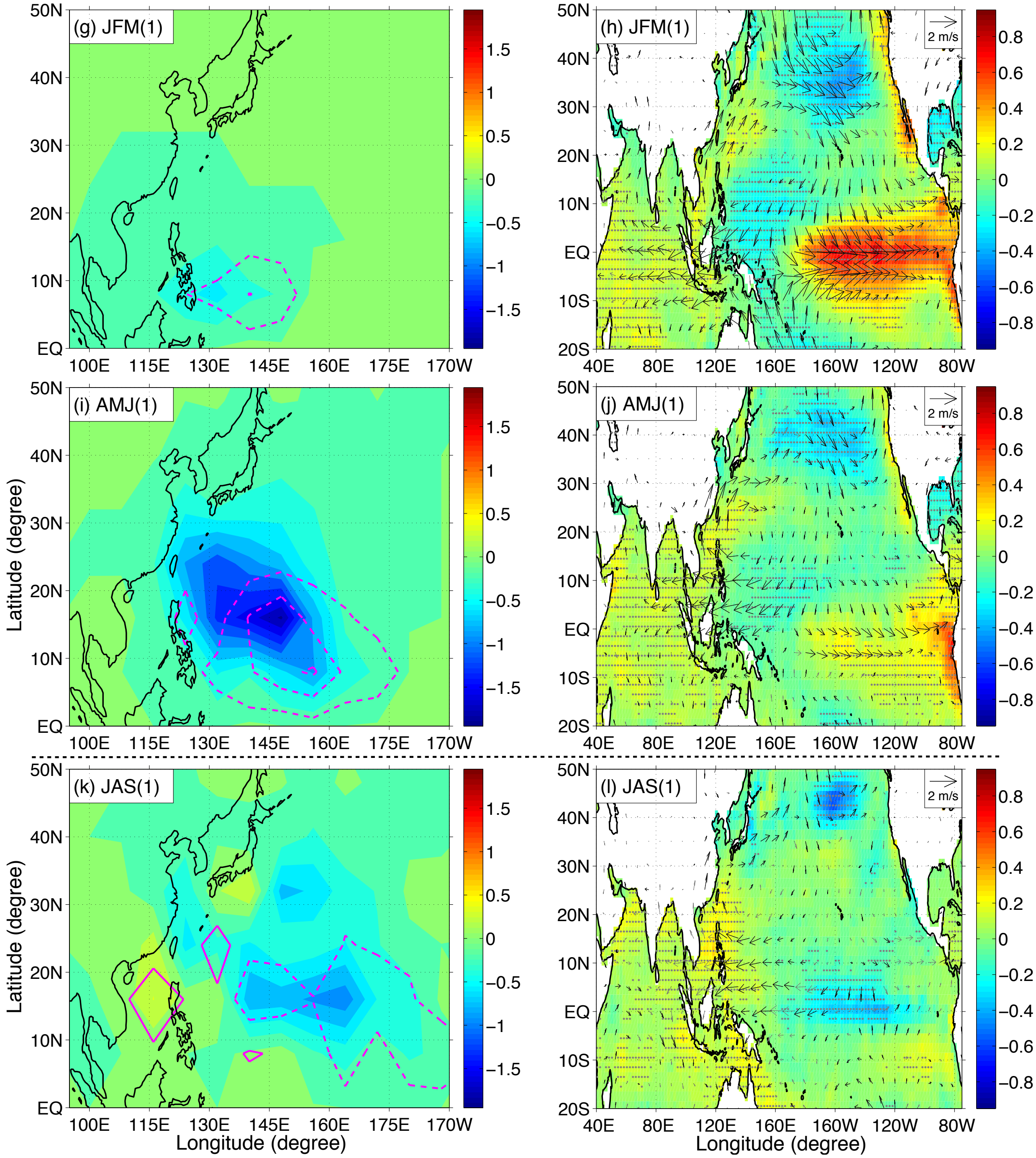

Figure 14: *Continued.*

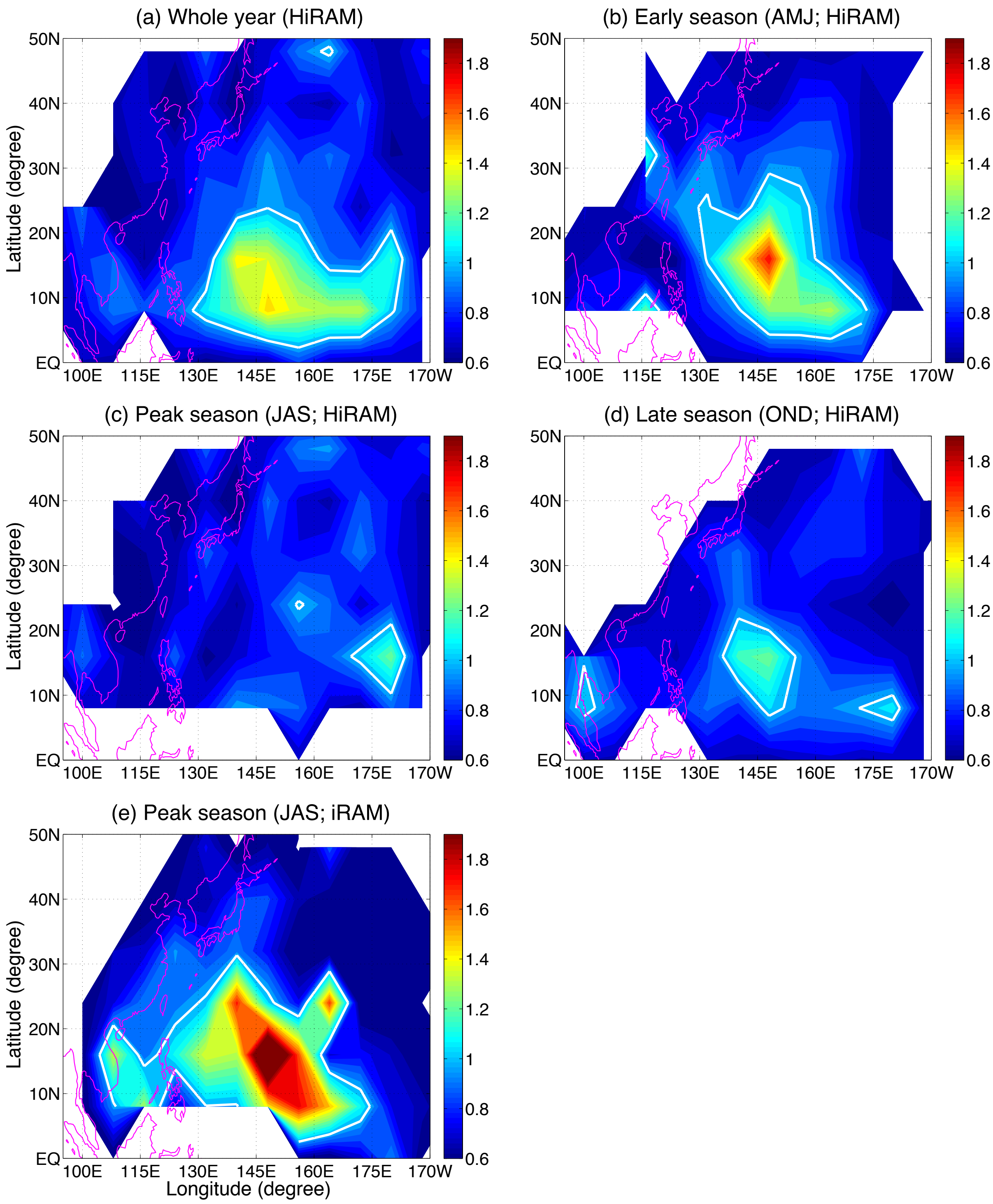

Figure 15: Signal-to-noise ratio for (a) annual, (b) early-season, (c) peak-season, and (d) late-season TC track density calculated based on an ensemble of three members of HiRAM simulations. (e) As in (c), but for the peak-season TC track density based on an ensemble of four members of iRAM simulations. White contours show values of 1.